



# Ultradeep ATCA Imaging of 47 Tucanae Reveals a Central Compact Radio Source

Alessandro Paduano<sup>1</sup> , Arash Bahramian<sup>1</sup> , James C. A. Miller-Jones<sup>1</sup> , Adela Kawka<sup>1</sup> , Tim J. Galvin<sup>1,2</sup> ,  
Liliana Rivera Sandoval<sup>3</sup> , Sebastian Kamann<sup>4</sup> , Jay Strader<sup>5</sup> , Laura Chomiuk<sup>5</sup> , Craig O. Heinke<sup>6</sup> ,  
Thomas J. Maccarone<sup>7</sup> , and Stefan Dreizler<sup>8</sup>

<sup>1</sup> International Centre for Radio Astronomy Research—Curtin University, 1 Turner Avenue, Bentley, WA 6102, Australia; [arash.bahramian@curtin.edu.au](mailto:arash.bahramian@curtin.edu.au)

<sup>2</sup> CSIRO Space & Astronomy PO Box 1130, Bentley, WA 6102, Australia

<sup>3</sup> Department of Physics and Astronomy, University of Texas Rio Grande Valley Brownsville, TX 78520, USA

<sup>4</sup> Astrophysics Research Institute, Liverpool John Moores University 146 Brownlow Hill, Liverpool L3 5RF, UK

<sup>5</sup> Center for Data Intensive and Time Domain Astronomy, Department of Physics and Astronomy, Michigan State University East Lansing, MI 48824, USA

<sup>6</sup> Department of Physics, University of Alberta CCIS 4-181, Edmonton, AB T6G 2E1, Canada

<sup>7</sup> Department of Physics & Astronomy, Texas Tech University Box 41051, Lubbock, TX 79409-1051, USA

<sup>8</sup> Institut für Astrophysik, Georg-August-Universität Göttingen Friedrich-Hund-Platz 1, D-37077 Göttingen, Germany

Received 2022 October 20; revised 2023 November 18; accepted 2023 November 19; published 2024 January 15

## Abstract

We present the results of an ultradeep radio continuum survey, containing  $\sim 480$  hr of observations, of the Galactic globular cluster 47 Tucanae with the Australia Telescope Compact Array. This comprehensive coverage of the cluster allows us to reach rms noise levels of  $1.19 \mu\text{Jy beam}^{-1}$  at 5.5 GHz,  $940 \text{ nJy beam}^{-1}$  at 9 GHz, and  $790 \text{ nJy beam}^{-1}$  in a stacked 7.25 GHz image. This is the deepest radio image of a globular cluster and the deepest image ever made with the Australia Telescope Compact Array. We identify ATCA J002405.702-720452.361, a faint ( $6.3 \pm 1.2 \mu\text{Jy}$  at 5.5 GHz,  $5.4 \pm 0.9 \mu\text{Jy}$  at 9 GHz), flat-spectrum ( $\alpha = -0.31 \pm 0.54$ ) radio source that is positionally coincident with the cluster center and potentially associated with a faint X-ray source. No convincing optical counterpart was identified. We use radio, X-ray, optical, and UV data to show that explanations involving a background active galactic nucleus, a chromospherically active binary, or a binary involving a white dwarf are unlikely. The most plausible explanations are that the source is an undiscovered millisecond pulsar or a weakly accreting black hole. If the X-ray source is associated with the radio source, the fundamental plane of black-hole activity suggests a black hole mass of  $\sim 54\text{--}6000 M_{\odot}$ , indicating an intermediate-mass black hole or a heavy stellar-mass black hole.

*Unified Astronomy Thesaurus concepts:* Black holes (162); Globular star clusters (656); Intermediate-mass black holes (816); Millisecond pulsars (1062); Radio astronomy (1338)

## 1. Introduction

### 1.1. Multiwavelength Sources in Globular Clusters

The Milky Way contains 158 known globular clusters (GCs; Baumgardt et al. 2019)—large, gravitationally bound clusters of stars that orbit the Galactic center. When compared to the Galactic field, it has been shown that X-ray binaries (XRBs), binary systems containing a black hole (BH) or a neutron star (NS), are overabundant in GCs when compared to the Galactic field (Clark 1975). This overabundance is due to the additional dynamical formation channels of XRBs in GCs (e.g., Fabian et al. 1975; Sutantyo 1975; Hills 1976).

It has been known for several decades that GCs contain a high number of X-ray-emitting sources (Clark et al. 1975). These initial detections spurred the first radio surveys of GCs using the NRAO interferometer (Johnson 1976; Johnson et al. 1977; Rood et al. 1978), the Arecibo 305 m telescope (Terzian & Conklin 1977), and the 100 m Effelsberg radio telescope. These initial radio surveys spanned frequency ranges of  $\sim 2\text{--}11$  GHz and were sensitive to bright sources with flux densities  $>1 \text{ mJy}$ . The discovery of millisecond pulsars (MSPs; Alpar et al. 1982) also spawned further radio timing surveys of GCs at lower frequencies to search for pulsars (Hamilton et al. 1985; Fruchter

& Goss 1990, 2000). Pulsars are abundant in GCs. To date, 257 pulsars are known in 36 GCs,<sup>9</sup> with Terzan 5 and 47 Tucanae containing the largest number of pulsars. Bayesian estimates indicate that there are potentially more than 2000 pulsars within Galactic GCs (Turk & Lorimer 2013).

Pulsars are not the sole class of radio sources that are expected to be detected in radio continuum imaging. Accreting XRBs, abundant in GCs, are expected to be visible at radio frequencies due to the radio synchrotron emission associated with nonthermal jets. Additionally, GCs are potentially hosts for the formation of intermediate-mass BHs (IMBHs) through a variety of different formation channels such as sequential mergers of stellar-mass BHs (Miller & Hamilton 2002) or the runaway growth of a massive object through stellar collisions (Portegies Zwart & McMillan 2002; Portegies Zwart et al. 2004). See Greene et al. (2020) for a recent review on IMBHs. This makes GCs prime targets in the search for IMBHs. An IMBH in a GC is assumed to accrete a portion of the gas within its sphere of influence, producing radio or X-ray emission that is potentially detectable (Maccarone 2004).

Due to the correlation among radio luminosity, X-ray luminosity, and mass (the fundamental plane of BH activity; Merloni et al. 2003; Falcke et al. 2004; Miller-Jones et al. 2012; Plotkin et al. 2012), the radio emission from an IMBH is expected to be brighter (at a given X-ray luminosity) than that from a stellar-mass BH. This makes radio continuum searches



Original content from this work may be used under the terms of the [Creative Commons Attribution 4.0 licence](https://creativecommons.org/licenses/by/4.0/). Any further distribution of this work must maintain attribution to the author(s) and the title of the work, journal citation and DOI.

<sup>9</sup> <https://www3.mpifr-bonn.mpg.de/staff/pfreire/GCpsr.html>

one of the best ways to try and detect IMBHs in GCs. Interpreting these searches involves making assumptions as to the radiative efficiency of any accretion onto an IMBH and the expected accretion rates (Pellegrini 2005), in addition to the expected gas density in GCs based on measurements using pulsar dispersion measures in 47 Tucanae (Freire et al. 2001; Abbate et al. 2018). Several papers have searched for IMBH accretion signatures in Galactic GCs (e.g., Maccarone 2005; Maccarone & Servillat 2008; Cseh et al. 2010; Lu & Kong 2011; Strader et al. 2012b; Tremou et al. 2018), with the most recent limits indicating that either IMBHs with masses  $\gtrsim 1000 M_{\odot}$  are not present in GCs, the accretion onto central IMBHs is more inefficient than predicted by Maccarone (2003), or that the gas density is lower in most clusters than in 47 Tucanae.

Recently, the first radio continuum imaging survey reaching mean noise levels  $< 10 \mu\text{Jy beam}^{-1}$  of 50 GCs in the Milky Way was conducted. The MAVERIC (Milky Way ATCA VLA Exploration of Radio Sources in Clusters) survey (Shishkovsky et al. 2020; Tudor et al. 2022) was a systematic survey of 50 Galactic GCs with the Karl G. Jansky Very Large Array (VLA) and the Australia Telescope Compact Array (ATCA) to assess the associated radio source populations. The pilot surveys revealed BH candidates in M22 (Strader et al. 2012a), M62 (Chomiuk et al. 2013), and 47 Tucanae (Miller-Jones et al. 2015), with the full survey detecting additional BH candidates in M10 (Shishkovsky et al. 2018) and NGC 6397 (Zhao et al. 2020) and transitional millisecond pulsar candidates in Terzan 5 (Bahramian et al. 2018) and NGC 6652 (Paduano et al. 2021). A new “hidden” MSP was also detected in NGC 6397 (Zhao et al. 2020), which has recently been confirmed by MeerKAT and Parkes timing (Zhang et al. 2022). As alluded to above, the full MAVERIC survey has been used to search for signatures of IMBH accretion in GCs (Strader et al. 2012b; Tremou et al. 2018). No IMBH signatures were detected in any GC in the MAVERIC sample.

### 1.2. Globular Cluster 47 Tucanae

After  $\omega$ -Centauri, 47 Tucanae (47 Tuc, NGC 104) is the second-brightest GC. It has a mass of  $\sim 8.95 \times 10^5 M_{\odot}$  and is located at a distance of  $4.52 \pm 0.03$  kpc (Baumgardt & Vasiliev 2021), with a very low extinction of  $E(B - V) = 0.04 \pm 0.02$  (Salaris et al. 2007). These last two points make the cluster an easy target for multiwavelength studies, with 47 Tuc being studied extensively by the Chandra X-ray Observatory and Hubble Space Telescope (HST). 47 Tuc contains a rich population of over 300 known X-ray sources of various classes, including low-mass X-ray binaries, cataclysmic variables (CVs), MSPs, and chromospherically active binaries (ABs) (Heinke et al. 2005; Bhattacharya et al. 2017). Of particular interest for this work is the X-ray source CXOG1b J002405.6–720452, also known as [GHE2001] W286 (hereafter W286,  $\alpha = 00:24:05.697$ ,  $\delta = -72:04:52.306$ ; Heinke et al. 2005; Bhattacharya et al. 2017), which falls within  $1''$  of the photometric center of 47 Tuc (as measured by Goldsbury et al. 2010). A potential optical counterpart was suggested for this source by Edmonds et al. (2003), corresponding to a BY Draconis variable Cl\* NGC 104 EGG V32 (hereafter PC1-V32,  $\alpha = 00:24:05.404$ ,  $\delta = -72:04:52.316$ ) first identified by Albrow et al. (2001), with a period of 1.64 days. BY Draconis (BY Dra) sources are main sequence variable stars that exhibit

luminosity variations due to chromospheric activity and the rotation of the star.

At the time of writing, 47 Tuc contained 29 known pulsars, which is the second largest number of pulsars in a GC behind Terzan 5. Nineteen pulsars are in binary systems, and 23 pulsars have phase-coherent timing solutions. The majority of the pulsars in 47 Tuc were discovered prior to 2003, with nine further sources identified and confirmed in the years since. Modeling by Ye et al. (2022) indicates that 47 Tuc may contain  $\sim 50$  MSPs, meaning there are potentially still several MSPs yet to be discovered in the cluster.

The existence of an IMBH in 47 Tuc has never been proven in previous literature. Freire et al. (2017) and Abbate et al. (2018) indicate that, based on the pulsar accelerations in the cluster, a central IMBH is not needed, with an upper limit on the mass of a central IMBH of  $\sim 4000 M_{\odot}$  (Abbate et al. 2018). Velocity dispersion modeling by Mann et al. (2019) found that the velocity dispersion in the core of the cluster can be produced by the binaries and BHs in the core, such that an IMBH is not needed to explain the velocity dispersion. They found an IMBH mass of  $40 \pm 1650 M_{\odot}$ , and that a central IMBH is only needed if the retention fraction of stellar-mass BHs and NSs is very low. Further multimass modeling by Hénault-Brunet et al. (2020) also indicates that an IMBH is not required in 47 Tuc to explain various observational constraints. Additional modeling of the cluster by Ye et al. (2022) indicated that approximately 200 BHs could be present, giving a total mass of BHs in 47 Tuc of  $\sim 2000 M_{\odot}$ . Most recently, Della Croce et al. (2023) analyzed the kinematics of the cluster’s central region and inferred that the observed kinematics are inconsistent with a central IMBH more massive than  $578 M_{\odot}$ .

The sheer number of X-ray sources in 47 Tuc makes it a very appealing target for radio continuum surveys. The first of these surveys was conducted by McConnell & Ables (2000) with the ATCA, reaching rms noise levels of 42 and  $46 \mu\text{Jy beam}^{-1}$  at 1.4 and 1.7 GHz, respectively, enabling the detection of 11 radio sources within  $5'$  of the cluster center. These 11 sources included the detections of two pulsars with known positions. This initial survey was built upon by Fruchter & Goss (2000), who presented images with rms noise levels of  $32 \mu\text{Jy beam}^{-1}$ . The initial survey by McConnell & Ables (2000) was extended to include 170 hr of ATCA data the following year, pushing the rms noise down to  $18 \mu\text{Jy beam}^{-1}$  (McConnell et al. 2001) and detecting nine radio sources in the cluster core. Following the bandwidth upgrade to the ATCA (Wilson et al. 2011), Lu & Kong (2011) obtained approximately 18 hr of ATCA data at 5.5 and 9 GHz in 2010, reaching an rms noise level of  $13.3 \mu\text{Jy beam}^{-1}$  after stacking both bands. These observations were subsequently combined with the MAVERIC observations of 47 Tuc, reaching rms noise levels of 4.4 and  $5.7 \mu\text{Jy beam}^{-1}$  at 5.5 and 9 GHz, respectively, and used to identify the BH candidate X9 (Miller-Jones et al. 2015). These radio continuum surveys have also contributed to placing mass upper limits on central IMBHs, with Lu & Kong (2011) and Tremou et al. (2018) using the fundamental plane of BH activity to place  $3\sigma$  upper mass limits of 520–4900  $M_{\odot}$  and 1040  $M_{\odot}$ , respectively. While both studies discussed the significant uncertainties associated with mass estimates derived from the fundamental plane, they did not account for this scatter (recently quantified as 1 dex by Gültekin et al. 2019) in their quoted mass limits.

In this paper, we combine the archival observations of Lu & Kong (2011) and Miller-Jones et al. (2015) with over 400 hr of new ATCA data to make the deepest radio image of a GC to date. Our ultradeep campaign reaches next-generation rms noise levels of  $\sim 790$  nJy beam $^{-1}$ , representing the deepest radio image ever made with the ATCA. The unparalleled depths that this imaging campaign reaches have allowed for the detection of a faint radio source (ATCA J002405.702-720452.361) at the photometric center of 47 Tuc. This paper will present an investigation of this radio source, and a follow-up paper will present the full radio source catalog from this campaign. In Section 2, we describe our radio observations and data reduction, in addition to other data analyzed during this study. The results are presented in Section 3. In Section 4, we provide a discussion of our findings and step through the possible source classes for ATCA J002405.702-720452.361. In Section 5, we present our conclusions.

## 2. Observations and Data Reduction

### 2.1. ATCA Observations

ATCA observed 47 Tuc under the project code C3427 over 41 epochs between 2021 March 31 and 2022 May 6. For all but five epochs, the array was in an extended 6 km configuration. This array configuration was chosen to maximize spatial resolution. For observations on 2021 December 28, 2021 December 30, 2022 January 2, and 2022 April 25, the array was in the 1.5 km configuration, and for 2022 May 6 the array was in the 750 m configuration. This was done to obtain shorter baseline coverage to improve our sensitivity to some extended sources in the field. A full overview of the date, duration, and array configuration of each epoch is shown in Table 1.

Observations were conducted in two bands simultaneously using the Compact Array Broadband Backend (CABB) correlator (Wilson et al. 2011). The two bands each had a bandwidth of 2048 MHz, split into equal 1 MHz channels, and were centered on frequencies of 5.5 and 9 GHz. The source B1934-638 was used as the primary calibrator for band-pass and flux calibration, and the source B2353-686 was used as the secondary calibrator for amplitude and phase calibration. Occasionally, the source J0047-7530 was used as the secondary calibrator for times where B2353-686 had set. During each observation, after initial calibration on B1934-638 for approximately 15 minutes, we cycled between observing the secondary calibrator and target for 1 minute and 15 minutes, respectively. During poorer observing conditions, the target integration time was reduced to 5 minutes between secondary calibrator scans.

### 2.2. Radio Data Reduction and Imaging

We reduced the data for each band separately. Data calibration was performed using standard procedures in MIRIAD (Sault et al. 1995) before we imported the *uv*-visibilities into the Common Astronomy Software Application (McMullin et al. 2007) for imaging. We used the `tclean` task for imaging and used a robust weighting factor of 1.0 to provide a good balance between image sensitivity and resolution. We used the multiterm multifrequency synthesis deconvolver with two Taylor terms to account for the frequency dependence of sources in the field, and the resulting images were primary beam corrected using the task `impbcor`. We used cell sizes of  $0''.3$  and  $0''.15$  and image sizes of 3072

and 5625 pixels for imaging the 5.5 and 9 GHz bands, respectively. The image center was set to approximately  $1'$  to the south of the cluster center. These image sizes and this image phase center offset were applied to aid in the reconstruction and deconvolution of some bright, extended sources toward the edge of the image field at 5.5 GHz.

Primary beam corrected images were made at both 5.5 and 9 GHz. We also imaged a co-stack of these two bands, which resulted in an image with an apparent central frequency of 7.25 GHz and a lower image noise than the separate bands. To create the deepest possible images, we stacked all 5.5 and 9 GHz epochs, excluding the data taken on 2021 April 7 and 2021 September 29 due to poor observing conditions. Again, we stacked and imaged both bands to produce a deep 7.25 GHz image of the field.

To verify that our imaging techniques in CASA were producing reliable results, we also imaged our data using DDFACET (Tasse et al. 2018). DDFACET performs spectral deconvolution using image-plane faceting. Given the small field of view of this campaign, and to improve computational efficiency, we imaged with four facets in a  $2 \times 2$  configuration. All other imaging parameters such as robustness, image size, and cell size were identical to those used in CASA. The images produced using DDFACET contained similar source distributions and noise structure, giving us confidence that our images were the correct representation of the data.<sup>10</sup>

#### 2.2.1. Archival Radio Data

To complement our survey, we searched the ATCA archive for previous observations of 47 Tuc. We combined our data with data taken by Lu & Kong (2011), Miller-Jones et al. (2015), and Bahramian et al. (2017), giving us an extra  $\sim 35$  hr of on-target observations. These data were reduced in the same manner described in Section 2.2. The inclusion of these data allowed us to reach rms noise levels of  $1.19 \mu\text{Jy beam}^{-1}$  at 5.5 GHz and  $940$  nJy beam $^{-1}$  at 9 GHz. When we stacked all the available data at 5.5 and 9 GHz together to make an image with an effective frequency of 7.25 GHz, the rms noise was  $790$  nJy beam $^{-1}$ , representing the deepest image made to date with the ATCA.

### 2.3. X-Ray Data

We used the X-ray source catalog of 47 Tuc compiled by Bhattacharya et al. (2017) as our main source catalog to search for potential X-ray counterparts to radio sources. To investigate the X-ray properties of 47 Tuc beyond the scope of Bhattacharya et al. (2017), we queried the Chandra archive for previous X-ray observations of the cluster using the Chandra/ACIS detector. Nineteen observations of 47 Tuc were made using the Chandra/ACIS detector between 2000 and 2015, totalling more than 500 ks of data that we obtained for our analysis.

For data reprocessing and analysis, we used CIAO 4.14 with CALDB 4.9.7 (Fruscione et al. 2006). All X-ray data were reprocessed using `chandra_repro` before stacking. To stack the observations, we first corrected the coordinate system of each observation by using `wavdetect` for source detection, and then `wcs_match` and `wcs_update` to create a matrix

<sup>10</sup> Furthermore, we found that the flux and spectral slope of the main target of this work (ATCA J002405.702-720452.361; see Section 3) were consistent between the two methods.



**Table 1**  
The ATCA Observations of 47 Tuc Taken Under the Project Code C3427

Date	Start Time (UTC)	Integration Time (hr)	Array Configuration
2021-03-31	21:00	11.66	6D
2021-04-01	20:00	11.56	6D
2021-04-05	22:00	9.63	6D
2021-04-07	01:30	9.12	6D
2021-04-08	21:30	10.87	6D
2021-04-09	20:30	11.54	6D
2021-04-11	20:00	11.58	6D
2021-04-14	17:00	11.53	6D
2021-04-15	20:00	11.45	6D
2021-04-16	17:00	11.50	6D
2021-04-17	20:00	11.69	6D
2021-04-23	23:00	10.00	6D
2021-06-29	18:30	9.72	6B
2021-06-30	17:30	10.83	6B
2021-07-01	17:30	10.62	6B
2021-09-09	06:00	11.52	6A
2021-09-12	09:00	11.49	6A
2021-09-17	05:00	11.20	6A
2021-09-19	12:00	11.24	6A
2021-09-20	10:00	11.35	6A
2021-09-21	08:30	11.48	6A
2021-09-22	08:30	11.56	6A
2021-09-23	08:30	12.40	6A
2021-09-25	07:30	11.62	6A
2021-09-26	09:00	11.36	6A
2021-09-28	06:00	11.97	6A
2021-09-29	08:30	9.64	6A
2021-10-01	07:30	11.68	6A
2021-11-17	13:00	2.75	6C
2021-11-22	07:00	8.91	6C
2021-12-28	06:00	7.68	1.5A
2021-12-30	02:00	11.75	1.5A
2022-01-02	02:00	10.11	1.5A
2022-01-22	00:30	11.68	6A
2022-01-26	00:00	5.31	6A
2022-01-27	00:00	11.41	6A
2022-01-28	00:00	11.96	6A
2022-01-30	00:00	12.82	6A
2022-01-30	23:30	13.81	6A
2022-04-25	18:00	11.53	1.5A
2022-05-06	15:30	13.64	750D

**Note.** For each epoch, the date and start time (in UTC), integration time, and array configuration are given.

transformation to apply and correct the World Coordinate System (WCS) parameters of each observation based on a single reference observation. When correcting the WCS parameters for stacking, we were only interested in the relative astrometry between each observation, as our main aim for this X-ray analysis was to extract X-ray spectra. Considerations of the absolute astrometry are outlined in Section 2.6. We used the task `merge_obs` to stack the observations.

Given that 47 Tuc had not been observed by Chandra since 2015 prior to our ATCA campaign, we obtained new Chandra data of the cluster to search for signs of significant X-ray variability. Under Director’s Discretionary Time (DDT), 47 Tuc was observed for 9.62 ks on 2022 January 26 (obs ID: 26229) and for 9.83 ks on 2022 January 27 (obs ID: 26286), giving us almost 20 ks of new Chandra data of 47 Tuc for the first time since 2015. These data were reprocessed via the same method described above, and also stacked with the archival Chandra data.

#### 2.4. HST Data

We used optical data from a variety of different sources in order to complement our survey and search for potential optical counterparts to radio sources detected. Primarily, we used data of 47 Tuc from the HST UV Globular Cluster Survey (HUGS; Piotto et al. 2015; Nardiello et al. 2018) to get an initial insight into the positions and properties of optical sources in the cluster. For further analysis, we used optical and UV data taken with the HST, specifically using the Space Telescope Imaging Spectrograph (STIS). STIS data were obtained from the Mikulski Archive for Space Telescopes. We used data under the program ID 8219 (PI: Knigge; Knigge et al. 2002), which were obtained between 1999 September 10 and 2000 August 16. Primarily, we looked at far-ultraviolet (FUV) data, which used the MIRFUV filter with the FUV-MAMA detector.

In this work, we also used near-ultraviolet (NUV) and optical data from General Observer Programs 12950 and 9281. The NUV dataset was taken on 2013 August 13 and contains

images in the F390W and F300X filters. The optical images were acquired over three visits on 2002 September 20, 2002 October 2/3, and 2002 October 11 in the F435W (B), F625W (R), and F658N ( $H\alpha$ ) filters. All images were calibrated and astrometrically corrected to the epoch J2000, as described in Rivera Sandoval et al. (2015), with point-spread function (PSF) photometry carried out, as mentioned in Rivera Sandoval et al. (2015, 2018). The optical data were aligned and photometrically analyzed using the software DOLPHOT (Dolphin 2016). Photometry was obtained using the individual FLC images in the three filters simultaneously, and we used the combined DRC image in the B filter as a reference frame. The magnitude limits are magnitude 27 for the NUV data, magnitude 24.5 for the R and  $H\alpha$  data, and magnitude 25 for the B data.

### 2.5. MUSE Integral Field Spectroscopy

The cluster 47 Tuc was observed with MUSE (Bacon et al. 2010) in narrow-field mode (NFM) during the night of 2019 November 1 for a total exposure time of  $4 \times 600$  s. In NFM, MUSE provides a field of view of  $7''.5 \times 7''.5$  with a spatial sampling of  $0''.025$  and uses the GALACSI module (Ströbele et al. 2012) in laser tomographic adaptive optics mode to achieve a spatial resolution of  $\lesssim 0''.1$ . The spectral coverage is from 470 to 930 nm with a constant FWHM of  $2.5 \text{ \AA}$ , corresponding to a spectral resolution of  $R \sim 1700\text{--}3500$ . The observations were taken as part of the MUSE guaranteed time observing (GTO) survey of GCs (PI: Kamann/Dreizler), described in Kamann et al. (2018).

The data were reduced with version 2.8.1 of the standard MUSE pipeline (Weilbacher et al. 2020). The pipeline performs the basic reduction steps (such as bias subtraction, flat-fielding, wavelength calibration, or flux calibration) on each individual exposure in order to create a pixtable, which contains the WCS coordinates, wavelength, flux, and flux uncertainty of every valid CCD pixel. In the last step, the individual pixtables are combined and resampled to the final data cube.

We extracted individual spectra from the data cube using PAMPELMUSE (Kamann et al. 2013). PAMPELMUSE uses a reference catalog of sources in the observed field in order to measure the positions of the resolved stars and the PSF as a function of wavelength. This information is then used in order to deblend the spectra of the individual stars from the cube. The reference catalog used in the analysis was published by Anderson et al. (2008) and is based on the HST/ACS survey of Galactic GCs presented in Sarajedini et al. (2007). In order to model the nontrivial shape of the MUSE PSF in NFM, we used the MAOPPY model by Fétick et al. (2019).

The extracted spectra were analyzed, as outlined in Husser et al. (2016). In particular, we measured stellar radial velocities from the extracted spectra by first cross correlating each of them against a synthetic template spectrum with matched stellar parameters and then performing a full-spectrum fit. The templates used to perform the cross correlation as well as the full-spectrum fitting were taken from the GLIB library presented in Husser et al. (2013). During the full-spectrum fitting, we also fitted for the effective temperature  $T_{\text{eff}}$  and the metallicity  $[M/H]$  of each star. The initial values for these parameters and the surface gravity  $\log g$  (which was fixed during the analysis) were obtained from a comparison of the HST photometry available in the reference catalog and isochrones from the Bressan et al. (2012) database.

In order to search for any resolved  $H\alpha$  emission, we further created a residuals map from the MUSE data in the wavelength range around 656.3 nm. To do so, we first subtracted the contribution of each resolved star using its spectrum, position in the cube, and the MAOPPY PSF model valid for each wavelength step. In order to suppress any artefacts from the extraction process (like PSF residuals or faint stars missing in the catalog), we also created the residuals map for two wavelength ranges bluewards and redwards of  $H\alpha$ . The two off-band residual maps were averaged and subtracted from the on-band residual map.

### 2.6. Astrometry

As we are combining data that have been taken several years apart, we need to consider the epochs that these data were taken in and shift the epochs in a manner such that the coordinates of different surveys can be compared. All source positions and surveys that we consider have coordinates in the equinox J2000.

The epoch of the radio data ranges from J2010.07 to J2022.34. To compare the coordinates of radio sources to other surveys from different epochs, we take the epoch of the radio data to be J2021.2, which corresponds to an average of all observation epochs weighted by the respective integration times.

The positions of the X-ray sources from Bhattacharya et al. (2017) were aligned in that paper with those of pulsars in the cluster based on Freire et al. (2003) and Freire et al. (2017), which are given in the epoch MJD 51600 ( $\sim$ J2000.16). The positions of optical sources from the HUGS survey are based on the epoch of Gaia DR1, which is J2015.0 (Nardiello et al. 2018). The position of the cluster center has been adopted from Goldsbury et al. (2010) for this work. This position has been astrometrically corrected to the 2MASS (Skrutskie et al. 2006) but does not appear to have been shifted to a particular epoch. Thus, the astrometry is likely to be the epoch at which the data were taken,  $\sim$ J2006.2.

To check the astrometric frame of the ATCA data, we identified 11 millisecond pulsars (PSR C, D, E, J, L, M, O, Q, S, T, U) whose positions and proper motions have been measured at high precision using pulsar timing observations (Freire et al. 2017), which are detected at  $>3\sigma$  in the ATCA dataset, and which are not confused with other sources. We transformed the timing positions from their measured epoch (J2000.16) to the adopted ATCA epoch (J2021.2). The median offsets in R.A. and decl., in the sense PSR–ATCA, are  $-0''.08 \pm 0''.05$  and  $+0''.04 \pm 0''.06$ , respectively, where the uncertainties listed are the standard errors of the mean. The weighted mean offsets in R.A. and decl. are consistent with these values, but slightly smaller, at  $-0''.05 \pm 0''.03$  and  $+0''.01 \pm 0''.05$ , where these are the uncertainties in the weighted means. The rms offsets in each coordinate are fully consistent with the median uncertainties in the ATCA positions of this sample. These comparisons suggest that (i) there is no evidence for an offset between the ATCA astrometry and the precise frame of the pulsars, and (ii) from this comparison alone, any offset is limited to  $0''.16$  at the  $2\sigma$  level.

Separately, we checked the absolute astrometry of the HUGS optical data by cross-checking with Gaia DR3, finding no evidence for an offset and an rms scatter of only  $\sim 0''.01$  for bright stars. We also compared the HUGS positions of the four millisecond pulsars (S, T, U, V) with known optical

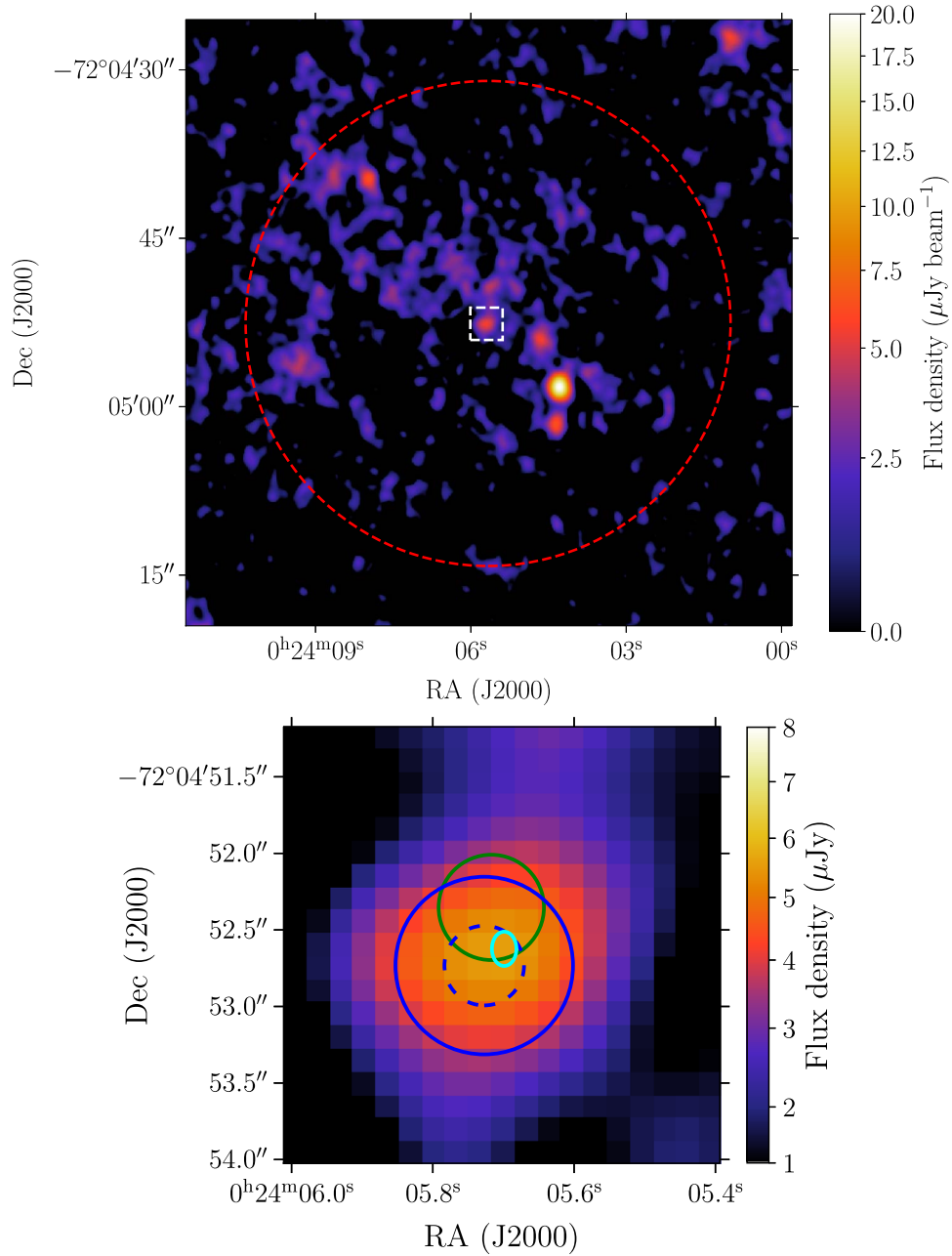


**Figure 1.** Top: 7.25 GHz radio image of 47 Tuc. The rms noise level in this image is  $\sim 790$  nJy beam $^{-1}$ . The core radius of 47 Tuc is shown by the dashed red circle. The white dashed box indicates the field of view of the bottom panel. Bottom: the  $1\sigma$  radio position of ATCA J002405 shown in cyan, compared to the 90% X-ray position of the source W286 (green), the cluster center uncertainty plus the Brownian motion radius added in quadrature for a  $6000 M_{\odot}$  BH (dashed blue circle), compared with the same radius for an illustrative  $570 M_{\odot}$  BH (solid blue circle). All coordinates are in the epoch of the radio image ( $\sim$ J2021.80). ATCA J002405 is within the uncertainty region of the X-ray source and the cluster center plus Brownian motion, even at the top end of the possible BH mass range.

counterparts (Rivera Sandoval et al. 2015) that are present in HUGS, finding very consistent astrometry between HUGS and the proper motion-corrected pulsar positions, with no evidence for an offset and an rms  $\lesssim 0''.01$ . Together, these checks show that the optical and radio frames are aligned to within a fraction of an HST pixel.

We rechecked the X-ray astrometry using the millisecond pulsars with precise positions and which Bhattacharya et al. (2017) identify as being relatively uncrowded in the X-ray (pulsars C, D, E, H, J, M, N, O, Q, T, U, W, Y, Z, ab). In R.A., there is indeed no offset (PSR–Chandra =  $0''.00 \pm 0''.01$ ), but we find evidence for a small offset in decl. of  $-0''.08 \pm 0''.02$ . The overall rms scatter in the PSR–Chandra coordinates is

$0''.07$ . This is much smaller than the formal 95% astrometric confidence intervals of the Chandra X-ray coordinates of the pulsars, which range from  $0''.30$  to  $0''.35$  (Bhattacharya et al. 2017). Hence, the uncertainty in the absolute astrometric frame of the X-ray data does not meaningfully affect our results. Nonetheless, given that the decl. offset is formally significant, we do apply this offset to the position of the source W286 discussed below.

For the remainder of the paper, to convert source positions to different epochs for comparison, we assume that the sources that are associated with the cluster move with the cluster proper motion of  $\mu_{\alpha} = 5.25$  mas yr $^{-1}$  and  $\mu_{\delta} = -2.53$  mas yr $^{-1}$ . These proper motion values have been adopted from Baumgardt et al. (2019),

**Table 2**

The Flux Density Measurements of ATCA J002405 at 5.5, 7.25, and 9 GHz Over the Course of the Survey

Subset	Frequency (GHz)	$S_\nu$ ( $\mu$ Jy)	rms ( $\mu$ Jy/beam)
Full survey	5.50	$6.3 \pm 1.2$	1.19
	7.25	$5.8 \pm 0.8$	0.79
	9.00	$5.4 \pm 0.9$	0.94
April (2021-03-31 to 2021-04-23)	5.50	$7.8 \pm 1.9$	1.88
	7.25	$6.5 \pm 1.3$	1.30
	9.00	$3.7 \pm 1.5$	1.48
September (2021-06-29 to 2021-10-01)	5.50	$5.9 \pm 1.7$	1.71
	7.25	$6.5 \pm 1.1$	1.11
	9.00	$7.5 \pm 1.3$	1.35
January (2021-11-17 to 2022-01-30)	5.50	$<6.87$	2.29
	7.25	$<4.50$	1.50
	9.00	$<5.52$	1.84

**Note.** The rms noise for each band is also listed. The chronological subsets were defined based on periods of intense observations in extended configurations, while compact configuration observations were used in imaging in all subsets. The flux density uncertainties also include the uncertainty due to the uncertainty in the calibration. The source was not detected in the January subset of our survey, so we list the  $3\sigma$  flux density upper limits in this case.

who derive the mean proper motions of Galactic GCs from Gaia DR2.

### 3. Results

#### 3.1. ATCA J002405.702-720452.361—A Possible Radio Counterpart to the X-Ray Source W286

Our deep ATCA imaging of 47 Tuc revealed a radio source, ATCA J002405.702-720452.361 (hereafter ATCA J002405), at the photometric center of the cluster, as taken from Goldsbury et al. (2010). The 7.25 GHz image of the core of the cluster is seen in the top panel of Figure 1. ATCA J002405 has a 5.5 GHz radio flux density of  $6.3 \pm 1.2 \mu$ Jy and a 9 GHz radio flux density of  $5.4 \pm 0.9 \mu$ Jy. The radio spectral index ( $S_\nu \propto \nu^\alpha$ ) is  $\alpha = -0.31 \pm 0.54$  and is consistent with being flat. Table 2 shows the flux density measurements of ATCA J002405 for each of the three main subsets of our campaign, in addition to the full campaign. As the source was not detected in the January subset of the survey, we list the  $3\sigma$  flux density upper limits of the source in Table 2. The source flux densities were measured using the CASA task `imfit` by assuming a point source model, and the  $3\sigma$  flux density upper limits were calculated by taking three times the central rms noise of each image.

The best position (in the epoch J2021.2) of ATCA J002405 is:

$$\begin{aligned} \text{R.A.} &= 00: 24: 05.7018 \pm 0.0173 \text{ s} \\ \text{Decl.} &= -72: 04: 52.631 \pm 0.112. \end{aligned}$$

This position was derived by using `imfit` to fit a point source model to the radio source, with uncertainties due to the thermal noise of the image. As shown in the bottom panel of Figure 1, ATCA J002405 is within the positional uncertainty region of

the X-ray source W286. Additionally, the angular distance between ATCA J002405 and the cluster center is  $0''.14$ , which is less than the sum in quadrature of the Brownian motion radius<sup>11</sup> for a  $6000 M_\odot$  BH (see Section 4.4 for details) and the positional uncertainty of the cluster center, which totals  $0''.26$ .

ATCA J002405 may also display variability on a timescale of several months. The source is detected in a stacked image in at least one of the frequency bands during the April and September subsets of our survey. It was not detected at  $>3\sigma$  in the January subset. However, this could be due to slightly higher noise compared to previous subsets (see Table 2). Thus, we cannot conclusively comment on nondetection being due to intrinsic variability or due to noise fluctuations.

#### 3.2. X-Ray Properties of W286

W286 was first identified as an X-ray source in 2005 (Heinke et al. 2005). To investigate the X-ray spectral properties of W286, we extracted a 0.3–10 keV X-ray spectrum from all the Chandra observations of 47 Tuc and combined them. A circular region with a radius of  $1''$  was chosen to extract source counts. An annulus with an inner radius of  $1''.7$  and an outer radius of  $10''$  was chosen to be the background region, although parts of this annulus were then excluded due to containing other X-ray sources. Source and background spectra were extracted using the CIAO task `specextract`, and the task `combine_spectra` was used to combine the individual spectra extracted for each observation into one stacked spectrum. Spectral analysis was performed using XSPEC 12.11.0 m (Arnaud 1996) and BXA (Buchner et al. 2014). The data were binned to have at least one count per bin, and fitting in XSPEC used C-stat statistics.

We fit three different models to the data: an absorbed power-law model (`tbabs × pegpwlw`), an absorbed blackbody radiation model (`tbabs × bbodyrad`), and an absorbed apec (Astrophysical Plasma Emission Code) model from diffuse ionized gas around the source (`tbabs × apec`). For all models, we froze the absorption parameter to the value of the hydrogen column density along the line of sight toward 47 Tuc, which is  $3.5 \times 10^{20} \text{ cm}^{-2}$ . This value is based on an  $E(B - V) = 0.04$  from the Harris catalog (Harris 1996), assuming  $R_V = 3.1$  and the  $N_H - A_V$  correlation from Bahramian et al. (2015); Foight et al. (2016). From the three models, the power-law model was the best-fitting model, with a photon index of  $\Gamma = 2.1 \pm 0.3$ , and giving a 0.5–10 keV X-ray luminosity of  $2.3^{+0.6}_{-0.5} \times 10^{30} \text{ erg s}^{-1}$ . A blackbody radiation model is the next best-fitting model with a relative probability to the power-law model of 0.79, followed by the apec model with a relative probability of 0.32. The fit parameters are shown in Table 3. The relative probabilities are calculated in BXA, which uses nested sampling to estimate the model evidence for each model fit, and then calculates relative probabilities.

We also visually inspected the X-ray spectrum to search for any distinctive features. In particular, we were searching for evidence of Fe L-shell emission, which can be a useful feature in identifying the source class of the object (e.g., ABs). The X-ray spectrum of W286 is shown in Figure 2, and also shows the best-fit power-law model and the residuals between the

<sup>11</sup> Estimated as  $\langle x^2 \rangle = (2/9)(M_*/M_{\text{BH}})r_c^2$ , where  $M_{\text{BH}}$  is the BH mass,  $M_*$  is the average mass of a star in the cluster core (taken to be  $\sim 1 M_\odot$ ), and  $r_c$  is the core radius of the cluster. (e.g., see Chandrasekhar 1943; Chatterjee et al. 2002; Lingam 2018).



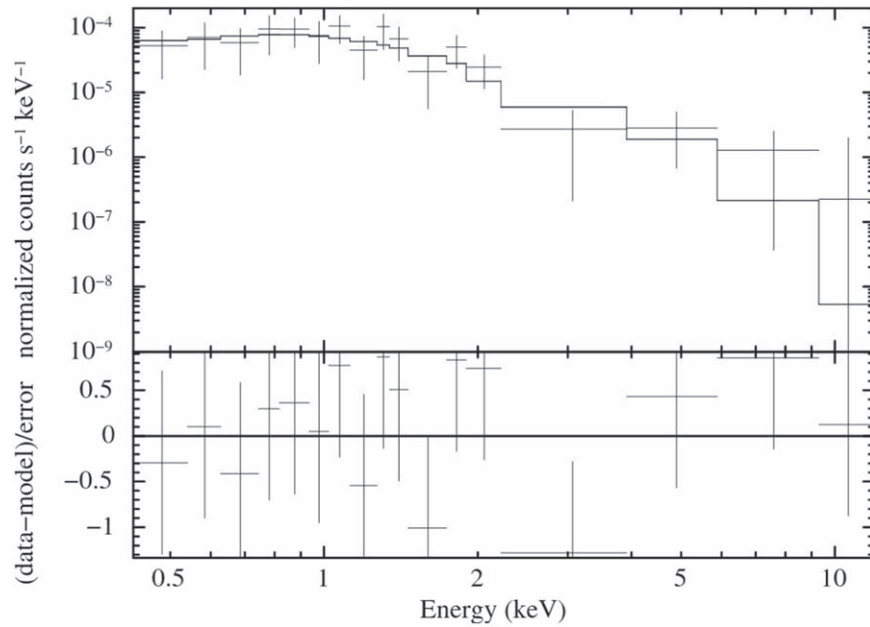


**Figure 2.** The X-ray spectrum of W286, fit with the best-fitting power-law model in the top panel. The bottom panel indicates the residuals between the model fit and the data. There is no evidence around 1 keV of Fe L-shell emission.

**Table 3**

The Best-fit Parameters of the Different X-Ray Spectral Models Fit to the Combined X-Ray Spectrum of W286

Spectral Fit	$\Gamma$	$\log(kT)$ (keV)	Relative Probability
Power law	$2.1 \pm 0.3$	...	1.00
Bbodyrad	...	$-0.5 \pm 0.1$	0.79
apec	...	$0.6 \pm 0.3$	0.32

**Note.** The photon index ( $\Gamma$ ) is listed in the case of the power-law model, and the electron temperature ( $\log(kT)$ ) is shown in the blackbody radiation and apec model cases. The relative probability indicates the probability of another model being preferred relative to the best-fitting model, which is the power-law model in this case. The relative probabilities are calculated using nested sampling to estimate the model evidence for each model fit.

model and the data. As can be seen, there is no evidence of an excess around 1 keV, where the Fe L-shell emission is expected. However, given the low number of source counts, any Fe L-shell emission may be too faint to be detected.

### 3.3. Optical and UV Properties of W286

To identify possible optical counterparts to ATCA J002405, we use a combination of the HUGS survey and the HST image from the F300X filter. Optical sources in the F300X image have a positional uncertainty of  $0''.074$ , as outlined in Rivera Sandoval et al. (2015). The F300X HST image of the cluster center is shown in Figure 3. We also consider the BY Dra PC1-V32 as a potential optical counterpart to ATCA J002405 given its previously claimed association with the X-ray source W286.

From the HUGS survey, we identify three potential HUGS sources whose localization and  $1\sigma$  error regions overlap with the  $1\sigma$  positional uncertainty of ATCA J002405: R0121449, R0121586, and R0121617. Expanding this to  $2\sigma$  includes PC1-V32 and the nearby HUGS source R0121517. PC1-V32 appears to be associated with the HUGS source R0121616, based on the available photometric information of both sources,

and is located outside the  $1\sigma$  uncertainty region of ATCA J002405. It is important to note that the sources R0121586 and R0121617 appear blended as one source. Upon further inspection, it is likely that the HUGS source R0121617 is not a real source. This source has no cluster membership information in the HUGS catalog and was identified in the F435W images in iteration six of the source finding. Upon further inspection of the individual images of the F435W and F336W filters and the subtracted images in the UV filters, there is no evidence of this source. This, in addition to only one source being detected in the region of the sources R0121617 and R0121586 in the F300X filter, means we are confident that R0121617 is not a real source.

To investigate the properties of these optical sources, we constructed color-magnitude diagrams (CMDs) of 47 Tuc for various combinations of filters. The filter combinations we considered were F390W versus F300X-F390W (UV),  $R$  versus  $H\alpha$ - $R$  ( $H\alpha$ ), and  $R$  versus  $B$ - $R$  (optical). These CMDs are shown in Figure 4. PC1-V32 (R0121616) shows some  $H\alpha$  excess and appears on the AB sequence in the  $H\alpha$  CMD and remains on the binary sequence in the UV CMD. R0121586 appears normal in the optical, UV, and  $H\alpha$ , and R0121449 is consistent with the main sequence in the optical and  $H\alpha$  CMDs, but near the binary sequence in the UV CMD.

We also used data from MUSE in NFM observations to investigate the optical sources in the X-ray uncertainty region. The narrow-band  $H\alpha$  image is shown in Figure 5, with the uncertainty regions of the cluster center, ATCA J002405, W286, and the optical sources indicated. This figure also shows the residual image after the removal of starlight. From this figure, there are no signs of any extended  $H\alpha$  emission above the detection limit, and no significant  $H\alpha$  source is detected at the location of ATCA J002405.

To complete our optical and UV analysis, we checked to see whether there was a prominent FUV source at the cluster center that was not present in the optical images. To do this, we visually inspected STIS images of the cluster. This indicated that there was no evidence of any source within our regions of



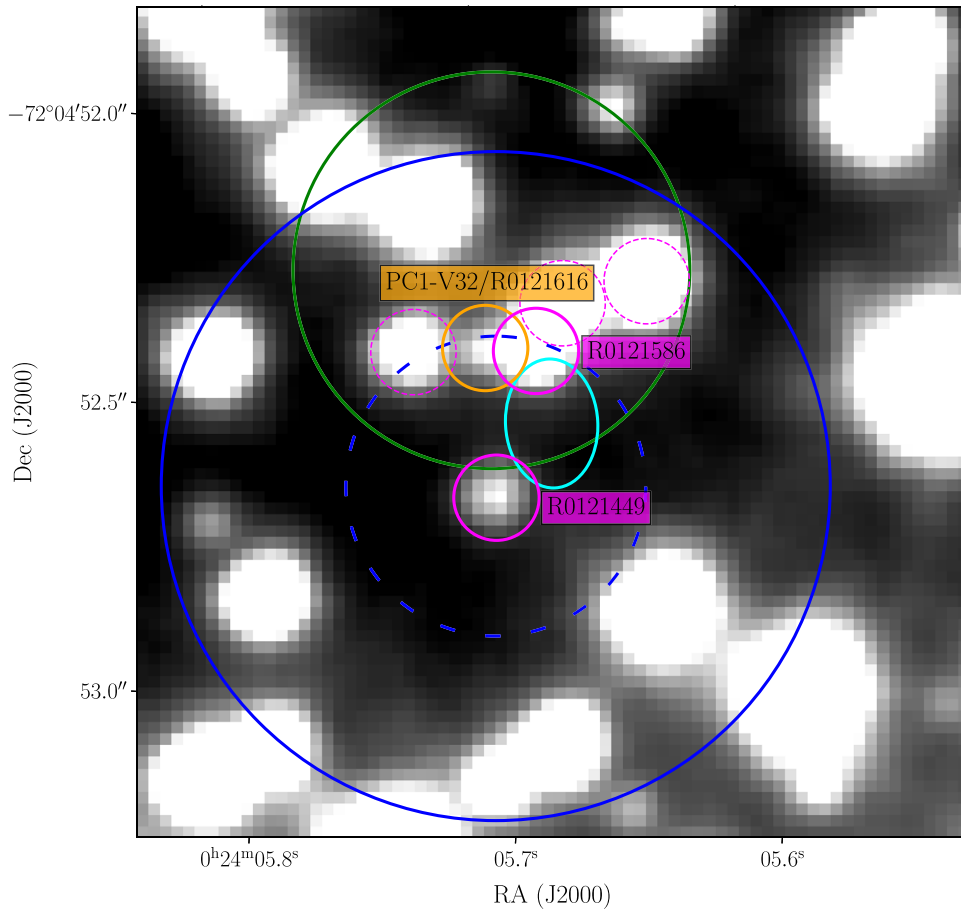


**Figure 3.** The UV (F300X) HST image of the cluster center, with positions of the radio source ATCA J002405 (cyan), X-ray source W286 (green), and the cluster center uncertainty and Brownian motion radius added in quadrature for a  $6000 M_{\odot}$  BH (dashed blue), and the same radius for an illustrative  $570 M_{\odot}$  BH (solid blue). All circles and ellipses are plotted with coordinates shifted to the epoch of the HST image, J2000. The magenta and orange circles represent positions of optical sources close to ATCA J002405. The solid magenta circles and labels indicate the HUGS sources whose positional uncertainties (represented by the size of the circles) overlap the  $1\sigma$  uncertainty ellipse of the radio source (excluding R0121617, which is unlikely to be real; see Section 3.3), with the dashed magenta circles indicating other nearby optical sources. The orange region and label represents the position of PC1-V32, which falls outside the radio uncertainty region.

interest down to a magnitude limit of  $\sim 24$  (the limiting magnitude given in the survey by Knigge et al. 2002).

## 4. Discussion

### 4.1. Possible Optical Counterparts

We investigated the possible optical counterparts to ATCA J002405, which include the two HUGS sources and PC1-V32, as mentioned in Section 3.3. Based on the available photometric data, PC1-V32 appears to be associated with the HUGS source R0121616. This source appears on the binary sequence in the  $H\alpha$  and UV CMDs, which is consistent with it being a BY Dra. PC1-V32 falls outside the  $1\sigma$  radio position, as seen in Figure 3, meaning that, while it remains possible, it is unlikely that the radio emission observed from ATCA J002405 is associated with PC1-V32. We discuss the radio properties of PC1-V32 and other ABs further in Section 4.3.2.

We now consider the two other counterparts identified in the HUGS survey, R0121449 and R0121586, as potential counterparts, as the uncertainty regions on these sources overlap with the radio uncertainty region of ATCA J002405. R0121449 has typical colors for its brightness in the optical and  $H\alpha$  CMDs, and indicates no evidence of accretion. However, the source appears to be consistent within errors with the binary sequence in the UV CMD, potentially indicating that it is a binary or

variable star. R0121586 is normal in the optical and the  $H\alpha$  CMDs, and falls in the scatter of the main sequence in the UV CMD, again showing no strong evidence for accretion. This latter source may also be consistent within errors with the binary sequence, for which there are two possible explanations. R0121586 could be a binary that has a slightly bluish component, or the photometry is affected by crowding and this slight shift to the binary sequence is caused by contamination from the nearby PC1-V32 rather than being intrinsic behavior of R0121586. These properties indicate that neither of these stars are obvious candidates for the source of the radio emission, and there is no obvious optical counterpart to our radio source.

### 4.2. The Origin of the X-Ray Emission

We used the MUSE data to investigate the other optical sources (specifically R0121449 and R0121586) within the X-ray uncertainty region to see if there were any glaring features from these sources that could explain the X-ray emission. The  $H\alpha$  and residual images are shown in Figure 5. Some of the optical sources have no spectra extracted because they are too faint, including the source that corresponds to PC1-V32. From this figure, there are no signs of any  $H\alpha$  emission above the detection limit. This indicates that none of these

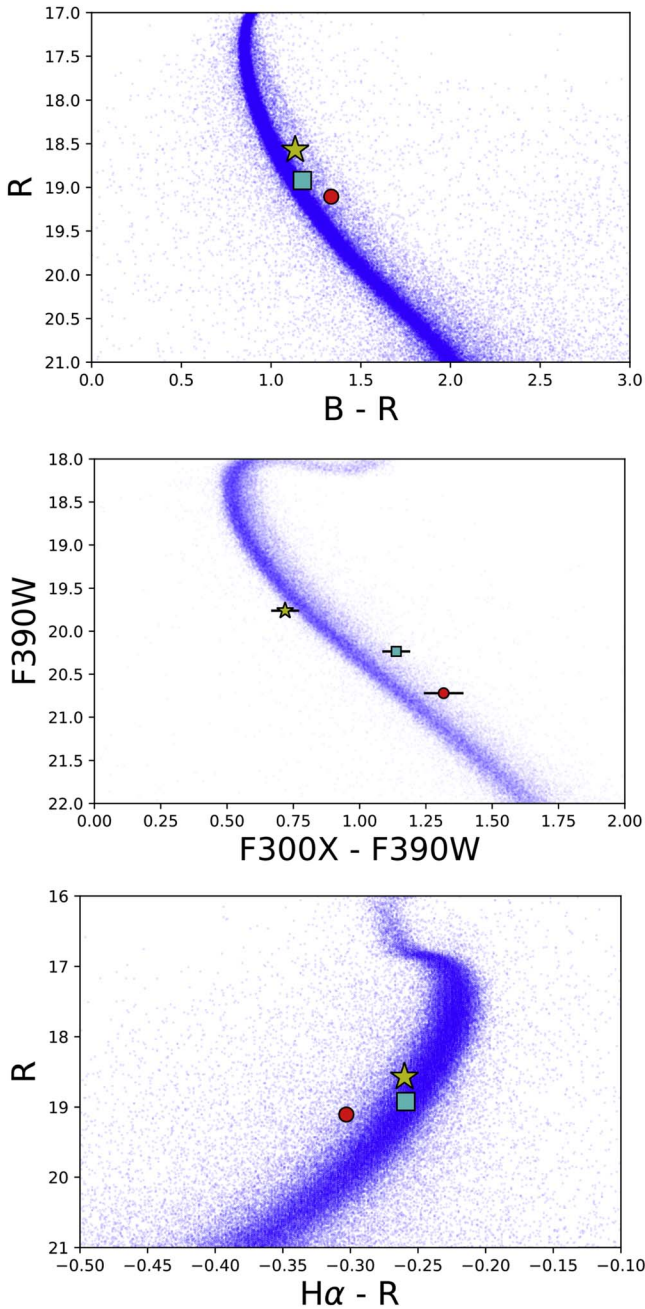


**Figure 4.** The optical, UV, and  $H\alpha$  CMDs of 47 Tuc, with our sources of interest also plotted. The BY Dra PC1-V32, which may be associated with the HUGS source R0121616, is denoted by the red circle, the HUGS source R0121449 is denoted by the cyan square, and the HUGS source R0121586 is denoted by the yellow star.

sources show clear evidence of any accretion present in the system. The extracted spectra of the stars within this region also show no strong evidence for  $H\alpha$  emission lines, again indicating that none of these sources are accreting. Overall, none of the optical sources in this field show glaring features in the MUSE data that could favor emission of X-rays via accretion or a similar process. This points to either ATCA J002405 or PC1-V32 being the source of the X-rays.

#### 4.3. Possible Radio Source Interpretations

Given the location of ATCA J002405 in a GC, there are several possible classifications for the source, depending on

whether the X-ray emission is associated with the radio source or some other source. By assuming that the X-ray source W286 is associated with ATCA J002405 and a cluster distance of 4.52 kpc (Baumgardt & Vasiliev 2021), we can plot the source on the radio/X-ray luminosity plane of accreting sources (Figure 6). ATCA J002405 falls well above the standard track for accreting stellar-mass BHs, and in a part of the parameter space that is occupied by the BH X-ray binary (BHXB) candidates in M22 and M62 (Strader et al. 2012a; Chomiuk et al. 2013) and unusual radio-bright white dwarf (WD) systems. We can use this to identify plausible source classes that could be responsible for this radio emission.

##### 4.3.1. Direct Current Offset in the Correlator

For our observations, we chose our pointing center prior to 2021 October 1 to coincide with that adopted by all other recent ATCA observations of the data, beginning with Lu & Kong (2011), for ease of stacking the data. However, this raises the possibility of a direct current (DC) offset in the correlator creating a spurious source at the phase center. If two waveforms are multiplied by a DC offset, then the offsets can produce a signal, even if there is no correlation between the two signals.

While a DC offset artifact has not yet been observed in data using the CABB correlator on the ATCA, as soon as we found evidence for a source at the cluster center, we took steps to minimize the possibility that this source could be caused by a system error. For all observations after 2021 October 1, we adjusted the pointing center of the 47 Tuc scans to the north by  $3''$ . An analysis of the stacked data after 2021 October 1 indicated that no source was detected at the pointing center of the imaged field. This, in addition to private communications with the ATCA Senior Systems Scientist regarding previous experience with the CABB correlator, means we are confident in ruling out a DC offset as the origin of ATCA J002405.

##### 4.3.2. Active Binary

ABs, tidally locked stars producing X-ray emission, make up a large portion of the X-ray sources in GCs below  $L_X < 10^{31} \text{ erg s}^{-1}$  (Güdel 2002). Furthermore, there is an observed relationship between the radio and X-ray emission of active stars of  $L_X/L_R \approx 10^{15}$  (Güdel & Benz 1993). We find it unlikely that ATCA J002405 is a type of AB. If we assume that the X-ray emission is associated with the radio source, the source becomes a radio-bright outlier on the Güdel-Benz relation, as shown in Figure 7, by about an order of magnitude. If the X-ray emission is not associated with the radio source, then the upper limit on the X-ray luminosity will decrease, making the source even more of an outlier on the Güdel-Benz relation.

Additionally, we have discussed the possibility of the BY Dra PC1-V32 being associated with ATCA J002405. For a comparison to the radio properties of ATCA J002405, we also assessed the radio luminosities of a larger group of BY Dra systems by constructing a sample based on radio and optical surveys. Our sample of BY Dra was chosen from the Zwicky Transient Facility (ZTF) catalog of variables (Bellm et al. 2019), as classified by Chen et al. (2020), who identified a total of 84,697 BY Dra systems. To confine our comparison to the most confident subset of these, we only select sources with at least 200 observations and a false alarm probability less than

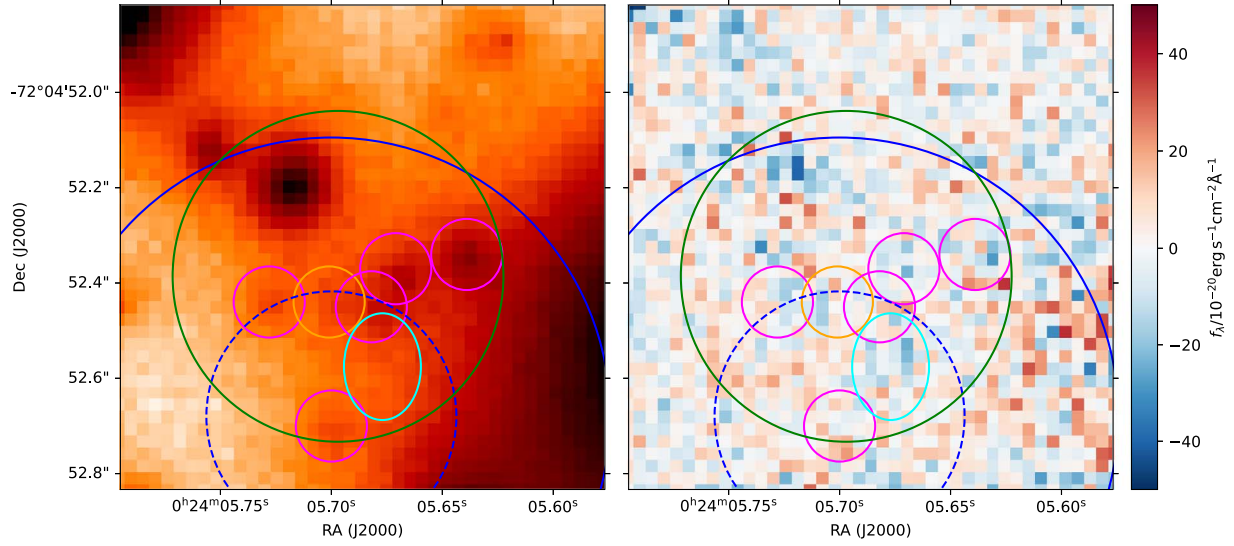


**Figure 5.** The left panel shows the narrow-band  $H\alpha$  image of 47 Tuc using a logarithmic flux map (flux mapped to increase from light colors to dark colors). The circles and ellipses shown in this image are the same as Figure 3. The right panel shows the residuals in  $H\alpha$  after the subtraction of stellar spectra, with the linear flux scale indicated by the color bar. Ellipses and circles are the same as shown in Figure 3. There is no evidence of a resolved  $H\alpha$  source in the regions considered.

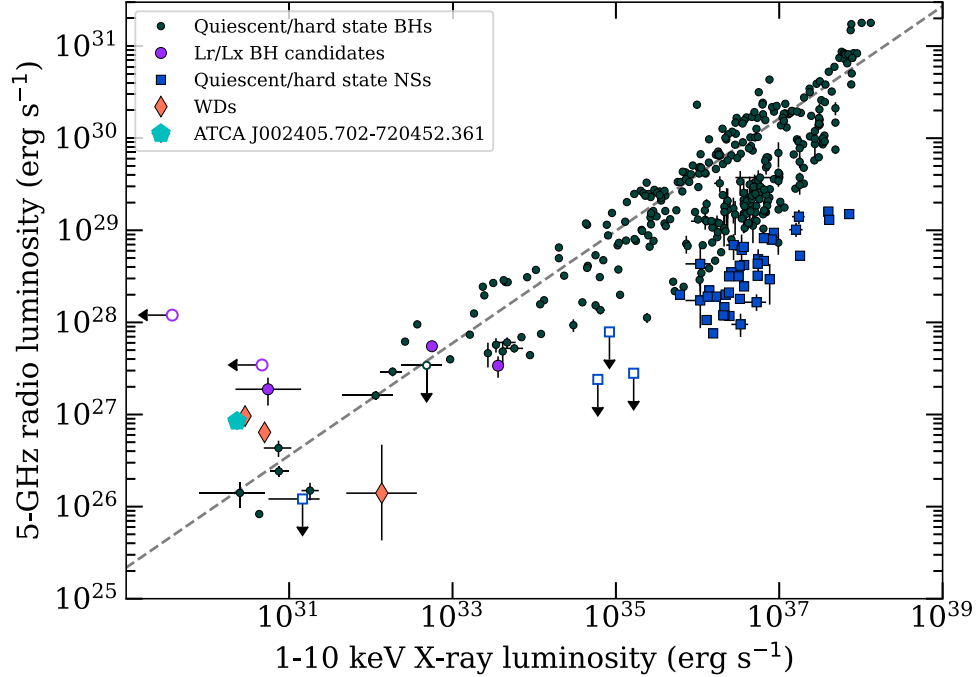


**Figure 6.** The radio/X-ray luminosity plane for several classes of stellar-mass accreting sources, compiled from Bahramian & Rushton (2022). The y-axis represents the quantity  $\nu L_\nu$ , where  $\nu = 5$  GHz. The dashed line in this figure indicates the  $L_R \propto L_X^{0.6}$  correlation for BHs from Gallo et al. (2014). Hollow markers with arrows represent upper limits. ATCA J002405 falls well above the standard track for accreting BHs, assuming that it is associated with the X-ray source W286 and assuming a distance to 47 Tuc of 4.52 kpc (Baumgardt & Vasiliev 2021). The error bars for this point are smaller than the marker size.

$10^{-5}$  in at least one band. This resulted in a total of 17,015 sources with a confident classification, and periods spanning from 0.15 to 44 days, fully encompassing the 1.64 days period of PC1-V32. We then cross-matched this subset with Gaia DR3 (Gaia Collaboration et al. 2023) using a coordinate offset threshold of  $0''.1$ , based on the estimated astrometric rms of the ZTF survey<sup>12</sup> (Masci et al. 2019), yielding 10,237 systems. Of these systems, we retained only sources with parallax significance  $>10\sigma$  and located  $<0.5$  kpc from Earth, such that

<sup>12</sup> Given that the Gaia and ZTF surveys have been performed close in time, effects of displacement by high proper motion are expected to be negligible.

wide-area radio surveys such as the Very Large Array Sky Survey (VLASS; typical sensitivity  $\sim 128$  to  $145 \mu\text{Jy beam}^{-1}$ ; Gordon et al. 2021) would be able to probe radio luminosities to sufficient depth. This resulted in a total of 1403 BY Dra systems with high confidence classification, tightly constrained distances within 500 pc, and relatively deep constraints on radio luminosity. We then obtained  $1' \times 1'$  cutout images around each source (using the NRAO VLASS Quick Look database<sup>13</sup>) and searched each of these cutouts statistically (searching for any pixels with peak flux densities above the  $3\sigma$

<sup>13</sup> <https://archive-new.nrao.edu/vlass/quicklook/>

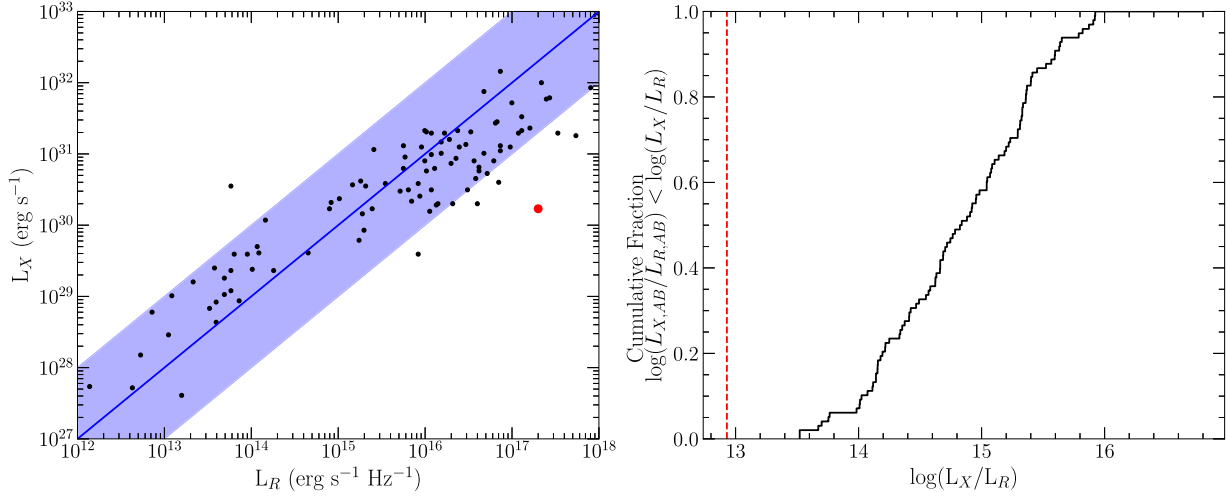


**Figure 7.** The left panel shows the radio/X-ray relation for active binaries from Guedel & Benz (1993). The red circle indicates our radio detection of ATCA J002405, and that it is outside the scatter of the correlation. The right panel indicates the cumulative fraction of ABs for various  $L_X/L_R$  fractions, with the red dashed lined indicating the  $L_X/L_R$  fraction of ATCA J002405.

of the  $1' \times 1'$  cutout) and inspected each visually to verify the presence/absence of a source. We found no significant radio sources within  $1''$  of any of these systems. Our  $3\sigma$  radio luminosity upper limits are computed from the rms values of the  $1' \times 1'$  cutout images for each individual source, and are shown in Figure 8. We also compare our results to V\* BY Draconis (the prototypical BY Dra variable), which is located at 16.5 pc with a consequently high proper motion of  $374.74 (\pm 0.04) \text{ mas yr}^{-1}$  (Gaia Collaboration et al. 2023). V\* BY Draconis is clearly detected in the VLASS survey at  $\sim 6 \text{ mJy}$ . However, this corresponds to a radio luminosity of  $\sim 2 \times 10^{15} \text{ erg s}^{-1} \text{ Hz}^{-1}$ , over two orders of magnitude radio-fainter than ATCA J002405, further reducing the likelihood that PC1-V32 is the origin of the radio emission. In summary, we find that BY Dra variables are extremely unlikely to show strong radio emission.

#### 4.3.3. Accreting White Dwarf

Accreting WDs also account for a large number of the X-ray-emitting sources in GCs (Grindlay et al. 2001; Pooley et al. 2002). Some WDs have been observed to reach the level of radio luminosity that we observe from ATCA J002405. However, these systems are only this radio bright during short radio flares and not persistently. While ATCA J002405 in 47 Tuc may display variability and is undetected in the January campaign of the survey, it was detected in April and September, and CV flares are not as long lasting as these individual month-long subsets of the survey, or the time between the April and September campaigns. Furthermore, the two optical sources consistent with the radio position of the source show no evidence of being a CV candidate or some other type of radio-bright WD as their colors are inconsistent with those of known WDs and CVs in 47 Tuc (Rivera Sandoval et al. 2018). Additionally, no CV has been identified at this position despite extensive monitoring. Thus, we find it unlikely that ATCA J002405 is a type of CV or other accreting WD. We do note, however, that photometry will be incomplete when going to fainter magnitudes at the center of 47 Tuc. This means that a faint optical counterpart could still be present, even though it is not seen in the HST data.

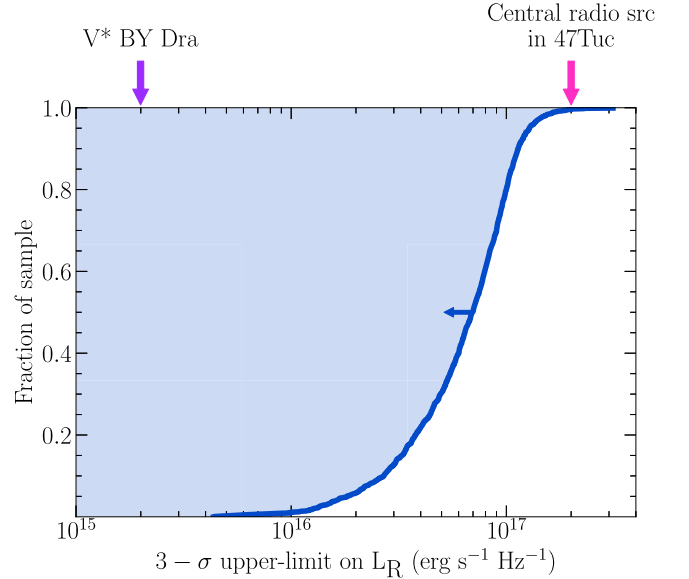


**Figure 8.** Cumulative distribution of radio luminosity upper limits for BY Dra variables in the sample investigated in this work. The purple arrow indicates the detected radio luminosity of V\* BY Draconis and the pink arrow indicates the radio luminosity of ATCA J002405 in 47 Tuc. No known BY Dra variable has radio luminosity comparable to ATCA J002405.

#### 4.3.4. Active Galactic Nucleus

Active galactic nuclei (AGNs) account for a large portion of background sources in the radio sky, meaning that it is entirely possible that ATCA J002405 is an AGN that happens to be coincident with the cluster center. However, it is unlikely that we would get a background AGN that is coincident with the center of 47 Tuc. When considering the background differential source counts from Wilman et al. (2008), the number of AGNs expected within one Brownian motion radius of the cluster center for a  $570 M_\odot$  BH when taking uncertainties into account ( $0.47''$ ) with a radio flux density greater than or equal to that of ATCA J002405 is  $4 \times 10^{-4}$ . This is shown in Figure 9. Even for a  $54 M_\odot$  BH, the expected number of AGNs remains less than  $4 \times 10^{-3}$ . This indicates that it is very unlikely that ATCA J002405 is a background AGN.



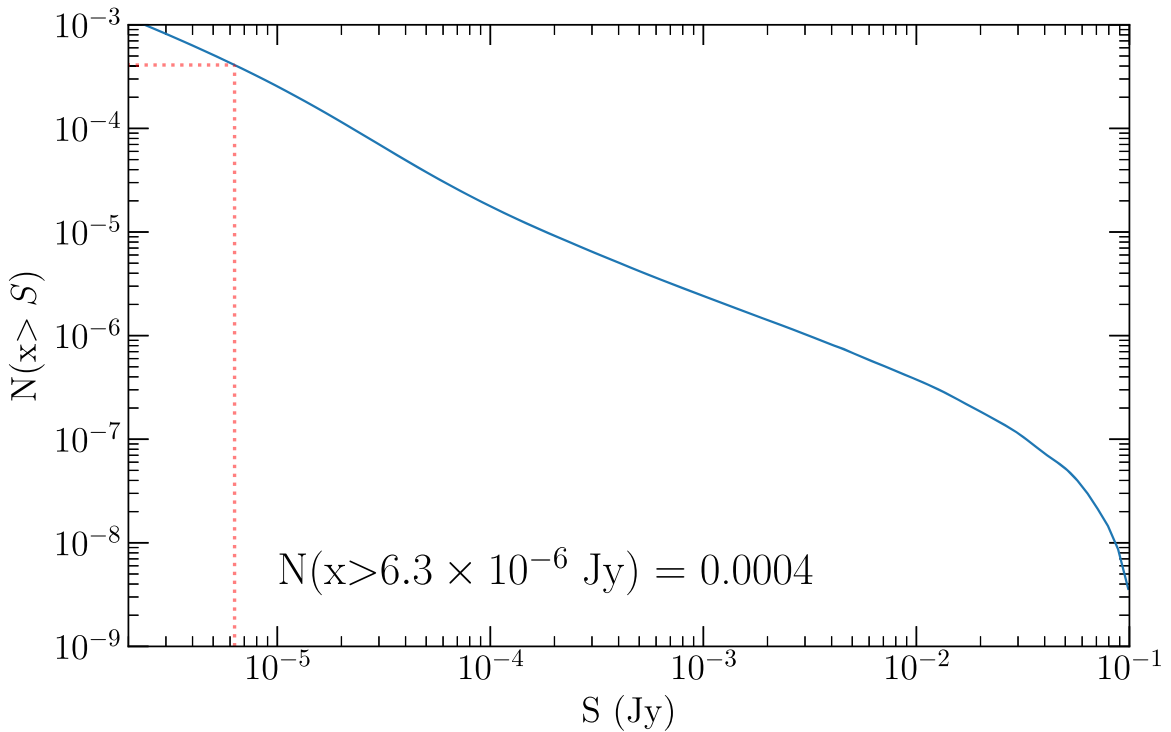


**Figure 9.** The number of AGNs we expect within the sky area of interest with a radio flux density greater than a given threshold plotted against flux density. The red dashed line indicates the 5.5 GHz radio flux density of ATCA J002405. We expect the number of AGNs within the sky area of interest with a flux density greater than this to be  $4 \times 10^4$ , making it unlikely that ATCA J002405 is an AGN.

#### 4.3.5. Pulsar

The GC 47 Tuc is known for containing a rich collection of pulsars, including MSPs and other isolated and spider pulsars. To date, there are 29 known pulsars in 47 Tuc.<sup>14</sup> As we will show in a future paper, we have detected several known pulsars in continuum imaging, meaning that it is possible we have detected a new pulsar very close to the cluster center. Such a source may not have been detected in previous pulsar surveys due to its faint radio flux density and the potential for it to be highly accelerated or hidden around part of its orbit. Spider pulsars, pulsars that are ablating their stellar companion, in particular can be hidden around parts of their orbit due to eclipsing or absorption (Roberts 2013).

The radio spectral index of ATCA J002405 is  $\alpha = -0.31 \pm 0.54$ , which, while consistent with a flat-spectrum object, is also consistent with the tail-end of the pulsar spectral index distribution. A recent examination of the radio spectra of Galactic MSPs by Aggarwal & Lorimer (2022) has shown that the population of MSPs has a mean spectral index of  $-1.3$  with a standard deviation of  $0.43$ . Further to this, Martsen et al. (2022) have shown that the MSPs in Terzan 5 have a spectral index distribution with a mean of  $-1.35$  and a standard deviation of  $0.53$ , indicating that the MSPs in GCs seem broadly consistent with the overall MSP population, as shown in Figure 10. The spectral index of ATCA J002405 is consistent with both of these distributions. The probability of obtaining a spectral index  $> -0.85$  (the lower uncertainty bound on our spectral index measurement) from the distribution of Aggarwal & Lorimer (2022) is  $0.14$ . Similarly, the probability of obtaining a spectral index  $> -0.85$  from the distribution of Martsen et al. (2022) is  $0.17$ . This indicates that,

based on its spectral index, ATCA J002405 could be an undiscovered pulsar at the center of the cluster. Further deep observations would be needed by other facilities such as MeerKAT to detect pulsations from and derive a timing solution for this potential pulsar. For a typical pulsar spectral index of  $-1.35$ , its predicted  $1.4$  GHz flux density would be  $40 \mu\text{Jy}$ , which, while faint, is within the range of pulsars previously detected in 47 Tuc (Camilo et al. 2000), while a flatter spectral index, as measured ( $-0.31$ ), would imply a  $1.4$  GHz flux density of only  $\sim 10 \mu\text{Jy}$ .

#### 4.3.6. Stellar-mass Black Hole

After decades of debate, we now know that GCs do contain stellar-mass BHs (e.g., Giesers et al. 2018, 2019). The ultracompact candidate BH X-ray binary 47 Tuc X9 resides within 47 Tuc (Miller-Jones et al. 2015; Bahramian et al. 2017), indicating that 47 Tuc may indeed contain some number of stellar-mass BHs. Modeling by Ye et al. (2022) has indicated that 47 Tuc could presently contain around 200 stellar-mass BHs, with a total BH mass in the cluster of  $\sim 2300 M_{\odot}$ . Due to the number of BHs expected in 47 Tuc, it is possible that ATCA J002405 is a stellar-mass BH in an XRB that has undergone some brightening. A Chandra DDT observation taken on 2022 January 26 and 27 indicates no increase in X-ray emission from W286 over what was detected in 2015 (albeit this nondetection also corresponds to the radio nondetection in the January subset of the observing campaign), and an analysis of Swift X-ray data over the past year shows no increase in total cluster X-ray luminosity, meaning a flaring X-ray transient  $> 10^{33} \text{ erg s}^{-1}$  can be ruled out.

On the radio/X-ray luminosity plane (Figure 6), ATCA J002405 falls above the standard correlation for accreting stellar-mass BHs. This is in the same part of the parameter

<sup>14</sup> <https://www3.mpifr-bonn.mpg.de/staff/pfreire/GCpsr.html>

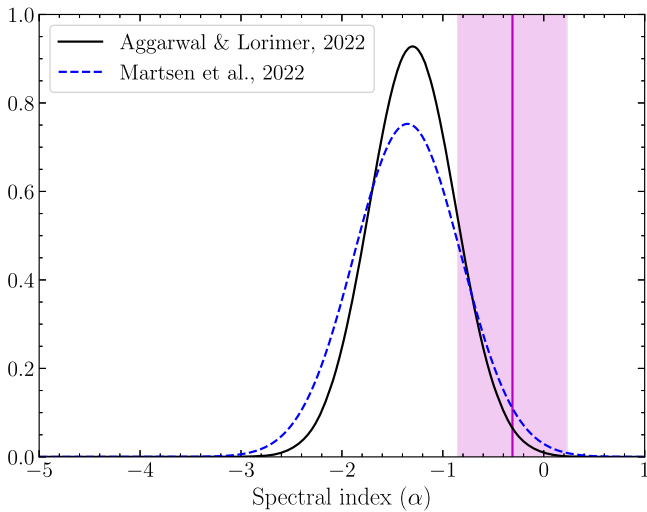


**Figure 10.** The spectral index distribution for a Galactic sample of MSPs from Aggarwal & Lorimer (2022), shown in black, and that for a sample of MSPs in Terzan 5 from Martsen et al. (2022), shown in blue. The radio spectral index of ATCA J002405 is shown as the magenta vertical line, with the shaded region indicating the  $1\sigma$  uncertainty on this value. The spectral index of ATCA J002405 is consistent with the tail-end of the pulsar spectral index distribution.

space as the stellar-mass BH candidates in the clusters M22 (Strader et al. 2012a) and M62 (Chomiuk et al. 2013), indicating that the radio/X-ray luminosity ratio of ATCA J002405 is similar to other BH candidates in clusters. Other stellar-mass BHs in quiescence have also been shown to occupy this part of the parameter space, specifically MAXI J1348-630 (Carotenuto et al. 2022). The radio spectrum of ATCA J002405 is consistent with being flat, which is what is expected from stellar-mass BHXBs. Furthermore, the best-fitting model to the X-ray spectrum of W286 is a power-law model with a photon index of  $\Gamma = 2.1 \pm 0.3$ . This means that, if W286 is associated with the radio source, its X-ray spectrum is consistent with an accreting BH in quiescence (Plotkin et al. 2017).

While the radio and X-ray properties of the source may be consistent with a stellar-mass BH, we have found no clear optical counterpart to ATCA J002405, although we again note that a counterpart too faint to be detected in HST data could have been missed. As discussed in Section 4.1, the two optical sources consistent with ATCA J002405 show no significant evidence of accretion or any significant discrepancy from the single star main sequence within uncertainties. This is at odds with what has been observed in other stellar-mass BHXB systems. For quiescent BHXBs, we would expect to observe some emission from the outer accretion disk. For example, the disk emission component in the X-ray transient A0620-00 is estimated as at least 10% of the total light in the near infrared (Cantrell et al. 2010). Thus, for an accreting BHXB, we would not expect the optical counterpart to fall on the main sequence of the cluster CMD. Due to this inconsistency in the optical properties of the source, we cannot conclusively confirm a stellar-mass BH as the classification of ATCA J002405, despite the supportive radio and X-ray behaviors.

#### 4.4. A Central Intermediate-mass Black Hole

The multiwavelength properties of ATCA J002405 do provide evidence that the source could be a candidate IMBH. The position of the source within the radius of Brownian motion of the photometric cluster center (Figure 3) is where

IMBHs in GCs would be expected to be located—they are the heaviest objects in the cluster and should have migrated to the cluster center by dynamical friction. The radio spectrum of the ATCA J002405 is also flat, consistent with what is expected for an IMBH in a low-luminosity state. Although ATCA J002405 does show evidence of variability, some radio variability is expected in quiescence (Plotkin et al. 2019) and has been observed previously in other BH systems, such as V404 Cygni and Sgr A\*.

We can make a rough estimate of the mass of any potential IMBH through the fundamental plane of BH activity. For consistency with previous works (e.g., Tremou et al. 2018), we adopt the following form of the fundamental plane with mass as the dependent variable, as shown in Miller-Jones et al. (2012):

$$\log M_{\text{BH}} = (1.638 \pm 0.070) \log L_R - (1.136 \pm 0.077) \log L_X - (6.863 \pm 0.790), \quad (1)$$

where the BH mass is in solar masses, and the radio and X-ray luminosities are in  $\text{erg s}^{-1}$ . We note that the uncertainties in the fit parameters are strongly correlated, such that standard error propagation of the terms in Equation (1) would overpredict the uncertainty on BH mass estimates.

For the case where the X-ray emission from W286 is associated with the radio emission from ATCA J002405, we can get a direct estimate of the BH mass from the radio and X-ray luminosities. The 5.5 GHz flux density of the source is  $6.3 \mu\text{Jy}$ , corresponding to a 5.5 GHz luminosity of  $8.47 \times 10^{26} \text{ erg s}^{-1}$  at a distance of 4.52 kpc (Baumgardt & Vasiliev 2021), and the 0.5–10 keV X-ray luminosity of W286 is then  $2.3 \times 10^{30} \text{ erg s}^{-1}$ . This corresponds to a position on the fundamental plane of  $570^{+430}_{-260} M_{\odot}$ , where the quoted uncertainty is purely statistical, and was calculated by considering only the errors on the radio and X-ray luminosities. However, the scatter on the fundamental plane will add further systematic uncertainty to this mass estimate. The most robust examination of the intrinsic scatter in the fundamental plane was performed by Gültekin et al. (2019). Through Markov Chain Monte Carlo simulations, Gültekin et al. (2019) found a systematic uncertainty in this relation of 0.96 dex. It is this more conservative estimate of  $\sim 1$  dex that we take to represent the intrinsic scatter in the fundamental plane. This means that our mass estimate of any BH is uncertain by at least a further order of magnitude, giving a nominal  $1\sigma$  mass range of  $\sim 54\text{--}6000 M_{\odot}$ .

Due to this scatter in the fundamental plane, our mass estimate cannot currently be made any more certain. It appears that the scatter in the mass direction for this relation is largely driven by supermassive BHs, and it is unknown how this scatter translates to lower-mass BHs such as IMBHs, which represent unexplored parts of the fundamental plane parameter space. Overall, despite its large intrinsic scatter, the fundamental plane still remains the only currently available method to estimate the mass of this source.

Within the cluster center, the Brownian motion radius for a BH can be estimated as  $\langle x^2 \rangle = (2/9)(M_*/M_{\text{BH}})r_c^2$ , where  $M_*$  is the average mass of a star in the cluster core (taken to be  $\sim 1 M_{\odot}$ ) and  $r_c$  is the core radius of the cluster<sup>15</sup> (see Strader et al. 2012b and Tremou et al. 2018). For the BH mass

<sup>15</sup>  $r_c$  is assumed to be 0.61 pc for 47 Tuc, based on Baumgardt & Vasiliev (2021).

**Table 4**  
Comparison of Explanations for the Origin of the Radio Emission

Source class	Possibility	Comment
Active binary	?	Radio emission is too bright for an active binary at this distance (Section 4.3.2)
White dwarf	?	Colors of optical counterparts are inconsistent with known WDs (Section 4.3.3)
AGN	?	Unlikely to have an AGN at this flux density this close to the cluster center (Section 4.3.4)
Stellar-mass BH	✓	$L_R/L_X$ ratio can be consistent with other BH candidates, no clear optical counterpart (Section 4.3.6)
Pulsar	✓✓	Spectral index is consistent with pulsar spectral index distribution (Section 4.3.5)
IMBH	✓✓	Radio source is located at the cluster center, mass estimates 54–6000 $M_\odot$ (Section 4.4)

constraint of 54–6000  $M_\odot$ , the resulting Brownian motion radii would be in the range  $0''.17$ – $2''.0$ , with the smallest Brownian motion radius corresponding to the highest mass. The source position lies within the combined uncertainty (summing in quadrature the Brownian motion radius and the uncertainty on the cluster center) of the cluster center, even for the smallest Brownian motion radius of  $0''.17$ .

The mass estimate above only considers the case where both the radio emission from ATCA J002405 and the X-ray emission from W286 are associated with a central IMBH. It is important to also consider the case where the X-ray emission from W286 is not associated with ATCA J002405 and is instead associated with PC1-V32, in which case we can again use the fundamental plane to estimate a BH mass lower limit. This can be calculated using the measured radio luminosity of the source and an upper limit on the X-ray luminosity from the source. Given that the radio source position falls within the uncertainty region of W286, we adopt the X-ray luminosity of W286 as the X-ray luminosity upper limit. This limit would lie at the same point on the fundamental plane relation as the direct measurement above, so in this case we adopt the BH mass lower limit (accounting for the scatter in the fundamental plane) of  $54 M_\odot$ . It is worth noting that a BH with a mass of  $54 M_\odot$  will have a Brownian radius of  $\approx 2''$ . This is large enough that the probability density of the BH being located so close to the cluster center would be low. This tentatively argues against the mass being quite this low.

It is also important to consider the case where both the radio emission from ATCA J002405 and the X-ray emission from W286 are not associated with a candidate IMBH. Because of the presence of a radio source within the Brownian motion region, it is possible that the radio emission from a potential IMBH could be hiding in the wings of the radio emission from ATCA J002405. In this case, we can use the flux density of ATCA J002405, an estimation of the X-ray emission expected from an IMBH accreting from the intracluster gas, and the fundamental plane relation to derive a mass upper limit for a central IMBH in 47 Tuc. This process follows the methodology outlined in Strader et al. (2012b) and Tremou et al. (2018). The X-ray luminosity of a source is related to its accretion rate ( $L_X = \epsilon \dot{M} c^2$ ) and, for accretion rates less than 2% of the Eddington rate, the radiative efficiency  $\epsilon$  scales with accretion rate (Maccarone 2003; Vahdat Motlagh et al. 2019) and can be expressed as

$$\epsilon = 0.1 \left( \frac{\dot{M}}{\dot{M}_{\text{Edd}}} / 0.02 \right). \quad (2)$$

The accretion rate  $\dot{M}$  is assumed to be some fraction of the Bondi accretion rate, usually  $\sim 0.03$  (Pellegrini 2005; Maccarone et al. 2007). To compute the Bondi accretion rate, we take the gas number density to be  $n = 0.2 \text{ cm}^{-3}$ , consistent

with pulsar measurements (Abbate et al. 2018). We also assume that the gas is fully ionized with a temperature  $T = 1 \times 10^4 \text{ K}$  and a mean molecular mass  $\mu = 0.59$ , which is typical for fully ionized gas (Fall & Rees 1985). For consistency with Strader et al. (2012b) and Tremou et al. (2018), we only consider the  $\gamma = 1$  isothermal case, although we note that the  $\gamma = 5/3$  adiabatic case will result in a higher mass upper limit.

Using the flux density of ATCA J002405 ( $6.3 \mu\text{Jy}$ ), the upper limit would then sit at  $860 M_\odot$  on the fundamental plane relation. This is lower than the corresponding fundamental plane estimate calculated by Tremou et al. (2018) due to the unparalleled image depth that we have achieved. However, to translate this to a true BH mass limit, we must again account for the intrinsic scatter in the fundamental plane relation, giving an upper limit on the BH mass of  $7900 M_\odot$ .

## 5. Conclusion

In this paper, we present the deepest radio image of the GC 47 Tucanae. Our ultradeep imaging campaign with the Australia Telescope Compact Array at 5.5 and 9 GHz has allowed us to reach an rms noise level of  $790 \text{ nJy beam}^{-1}$ , representing the deepest radio continuum image made of a GC and the deepest radio image ever made by the Australia Telescope Compact Array.

Based on analysis of these data, we have identified ATCA J002405.702-720452.361, a flat-spectrum, variable radio source that falls within the uncertainty region of the faint X-ray source W286 and the cluster center. This source has a 5.5 GHz flux density of  $6.3 \pm 1.2 \mu\text{Jy}$  and a spectral index of  $\alpha = -0.31 \pm 0.54$ . We consider several possible explanations for the origin of the radio and X-ray emission, and conclude that the radio source does not originate from the previously proposed counterpart to W286, a BY Draconis source (PC1-V32), and that the X-ray emission from W286 is associated with either PC1-V32 or this newly discovered radio source. We consider several possible source class explanations for ATCA J002405.702-720452.361, which are summarized in Table 4, and we find that the most likely classifications for the source are either an undiscovered pulsar or an IMBH. A stellar-mass BH appears less likely than these other explanations but cannot be ruled out.

It is not unsurprising that a pulsar at the cluster center may have been missed. ATCA J002405.702-720452.361 is very faint, meaning that it may have been invisible to previous low-frequency pulsar surveys of 47 Tucanae. Additionally, the pulsar could be highly accelerated or hidden for parts of its orbit, either through absorption or eclipsing by a binary companion, again rendering it invisible. Further deep observations with MeerKAT would be needed to fully explore this possibility, in addition to potential higher- or lower-frequency



detections to attempt to further constrain the spectral index of the source. These observations would allow us to test whether ATCA J002405.702-720452.361 is another member of 47 Tucanae's large pulsar population.

In the event that ATCA J002405.702-720452.361 is an IMBH, we use the fundamental plane of BH activity to estimate the mass of the source. In the event that the radio and X-ray emission are associated, the source location on the fundamental plane would sit well below previous upper limits on BH mass. Accounting for the  $\sim 1$  dex intrinsic scatter on the fundamental plane, we find a  $1\sigma$  uncertainty range on the BH mass of 54–6000  $M_\odot$ . This can be further reduced at the upper end by considering the kinematic studies of the central region of the cluster (Della Croce et al. 2023; see Section 1.2) to give a mass range of 54–578  $M_\odot$ . An IMBH with mass  $\leq 578 M_\odot$  would have a sphere of influence of  $\leq 0''.8$ . A better mass estimate for any central BH could be achieved if an orbiting companion is identified, allowing for the mass to be dynamically measured. It would be valuable to get proper motions for as complete as possible a sample of stars within this sphere of influence, either with ground-based adaptive optics data or with the James Webb Space Telescope. This would allow the presence of a central IMBH to be tested, either through dynamical modeling or through searching for a potential companion star.

### Acknowledgments

We would like to thank the anonymous referee for useful comments on the manuscript. A.P. would like to thank Jamie Stevens and the other support staff and duty astronomers responsible for the operation of the Australia Telescope Compact Array for their help and assistance during this observing campaign. Additionally, A.P. would like to thank the director of the Chandra X-ray Observatory, Patrick Slane, for approving a request for Director's Discretionary Time, and the support staff at the Chandra X-ray observatory for their assistance in performing this observation. A.P. would also like to acknowledge Freya North-Hickey and Ben Quici for useful discussions about data reduction procedures, Chris Riseley and Cyril Tasse for useful discussions involving imaging and self-calibration, Cath Trott for useful discussions regarding error propagation, and Maureen van den Berg for useful discussions regarding photometry. C.O.H. thanks Greg Sivakoff for useful discussions.












A.P. was supported by an Australian Government Research Training Program (RTP) Stipend and RTP Fee-Offset Scholarship through Federation University Australia. S.K. acknowledges funding from UKRI in the form of a Future Leaders Fellowship (grant No. MR/T022868/1). J.S. acknowledges support from NASA grant 80NSSC21K0628 and the Packard Foundation. C.O.H. is supported by NSERC Discovery Grant RGPIN-2016-04602.

The Australia Telescope Compact Array is part of the Australia Telescope National Facility, which is funded by the Australian Government for operation as a national facility managed by CSIRO. We acknowledge the Gomeri people as the traditional owners of the observatory site.

**Facilities:** Australia Telescope Compact Array, Chandra X-ray Observatory, Hubble Space Telescope, MUSE.

**Software:** Astropy (Astropy Collaboration et al. 2018), CASA (McMullin et al. 2007), CIAO (Fruscione et al. 2006), DDFacet (Tasse et al. 2018), Miriad (Sault et al. 1995), Matplotlib (Hunter 2007), Numpy (Harris et al. 2020).

### ORCID iDs

Alessandro Paduano  <https://orcid.org/0000-0003-0725-8330>  
 Arash Bahramian  <https://orcid.org/0000-0003-2506-6041>  
 James C. A. Miller-Jones  <https://orcid.org/0000-0003-3124-2814>  
 Adela Kawka  <https://orcid.org/0000-0002-4485-6471>  
 Tim J. Galvin  <https://orcid.org/0000-0002-2801-766X>  
 Liliana Rivera Sandoval  <https://orcid.org/0000-0002-9396-7215>  
 Sebastian Kamann  <https://orcid.org/0000-0001-6604-0505>  
 Jay Strader  <https://orcid.org/0000-0002-1468-9668>  
 Laura Chomiuk  <https://orcid.org/0000-0002-8400-3705>  
 Craig O. Heinke  <https://orcid.org/0000-0003-3944-6109>  
 Thomas J. Maccarone  <https://orcid.org/0000-0003-0976-4755>  
 Stefan Dreizler  <https://orcid.org/0000-0001-6187-5941>

### References

- Abbate, F., Possenti, A., Ridolfi, A., et al. 2018, *MNRAS*, **481**, 627  
 Aggarwal, K., & Lorimer, D. R. 2022, arXiv:2203.05560  
 Albrow, M. D., Gilliland, R. L., Brown, T. M., et al. 2001, *ApJ*, **559**, 1060  
 Alpar, M. A., Cheng, A. F., Ruderman, M. A., & Shaham, J. 1982, *Natur*, **300**, 728  
 Anderson, J., Sarajedini, A., Bedin, L. R., et al. 2008, *AJ*, **135**, 2055  
 Arnaud, K. A. 1996, in ASP Conf. Ser. 101, *Astronomical Data Analysis Software and Systems V*, ed. G. H. Jacoby & J. Barnes (San Francisco, CA: ASP), 17  
 Astropy Collaboration, Price-Whelan, A. M., Sipőcz, B. M., et al. 2018, *AJ*, **156**, 123  
 Bacon, R., Accardo, M., Adjali, L., et al. 2010, *Proc. SPIE*, **7735**, 773508  
 Bahramian, A., Heinke, C. O., Degenaar, N., et al. 2015, *MNRAS*, **452**, 3475  
 Bahramian, A., Heinke, C. O., Tudor, V., et al. 2017, *MNRAS*, **467**, 2199  
 Bahramian, A., & Rushton, A. 2022, *bersavosh/VRB-LrLx\_pub*: update 20220908, v220908, Zenodo, doi:10.5281/zenodo.7059313  
 Bahramian, A., Strader, J., Chomiuk, L., et al. 2018, *ApJ*, **864**, 28  
 Baumgardt, H., Hilker, M., Sollima, A., & Bellini, A. 2019, *MNRAS*, **482**, 5138  
 Baumgardt, H., & Vasiliev, E. 2021, *MNRAS*, **505**, 5957  
 Bellm, E. C., Kulkarni, S. R., Graham, M. J., et al. 2019, *PASP*, **131**, 018002  
 Bhattacharya, S., Heinke, C. O., Chugunov, A. I., et al. 2017, *MNRAS*, **472**, 3706  
 Bressan, A., Marigo, P., Girardi, L., et al. 2012, *MNRAS*, **427**, 127  
 Buchner, J., Georgakakis, A., Nandra, K., et al. 2014, *A&A*, **564**, A125  
 Camilo, F., Lorimer, D. R., Freire, P., Lyne, A. G., & Manchester, R. N. 2000, *ApJ*, **535**, 975  
 Cantrell, A. G., Bailyn, C. D., Orosz, J. A., et al. 2010, *ApJ*, **710**, 1127  
 Carotenuto, F., Corbel, S., & Tzioumis, A. 2022, *MNRAS*, **517**, L21  
 Chandrasekhar, S. 1943, *ApJ*, **97**, 255  
 Chatterjee, P., Hernquist, L., & Loeb, A. 2002, *ApJ*, **572**, 371  
 Chen, X., Wang, S., Deng, L., et al. 2020, *ApJS*, **249**, 18  
 Chomiuk, L., Strader, J., Maccarone, T. J., et al. 2013, *ApJ*, **777**, 69  
 Clark, G. W. 1975, *ApJL*, **199**, L143  
 Clark, G. W., Markert, T. H., & Li, F. K. 1975, *ApJL*, **199**, L93  
 Cseh, D., Kaaret, P., Corbel, S., et al. 2010, *MNRAS*, **406**, 1049  
 Della Croce, A., Pascale, R., Giunchi, E., et al. 2023, arXiv:2310.15221  
 Dolphin, A., 2016, DOLPHOT: Stellar photometry, Astrophysics Source Code Library, ascl:1608.013  
 Edmonds, P. D., Gilliland, R. L., Heinke, C. O., & Grindlay, J. E. 2003, *ApJ*, **596**, 1177  
 Fabian, A. C., Pringle, J. E., & Rees, M. J. 1975, *MNRAS*, **172**, 15  
 Falcke, H., Kording, E., & Markoff, S. 2004, *A&A*, **414**, 895  
 Fall, S. M., & Rees, M. J. 1985, *ApJ*, **298**, 18  
 Fétick, R. J. L., Fusco, T., Neichel, B., et al. 2019, *A&A*, **628**, A99  
 Foight, D. R., Güver, T., Özel, F., & Slane, P. O. 2016, *ApJ*, **826**, 66  
 Freire, P. C., Camilo, F., Kramer, M., et al. 2003, *MNRAS*, **340**, 1359  
 Freire, P. C., Kramer, M., Lyne, A. G., et al. 2001, *ApJL*, **557**, L105  
 Freire, P. C. C., Ridolfi, A., Kramer, M., et al. 2017, *MNRAS*, **471**, 857  
 Fruchter, A. S., & Goss, W. M. 1990, *ApJL*, **365**, L63  
 Fruchter, A. S., & Goss, W. M. 2000, *ApJ*, **536**, 865



- Fruscione, A., McDowell, J. C., Allen, G. E., et al. 2006, *Proc. SPIE*, **6270**, 62701V
- Gaia Collaboration, Vallenari, A., Brown, A. G. A., et al. 2023, *A&A*, **674**, A1
- Gallo, E., Miller-Jones, J. C. A., Russell, D. M., et al. 2014, *MNRAS*, **445**, 290
- Giesers, B., Dreizler, S., Husser, T.-O., et al. 2018, *MNRAS*, **475**, L15
- Giesers, B., Kamann, S., Dreizler, S., et al. 2019, *A&A*, **632**, A3
- Goldsbury, R., Richer, H. B., Anderson, J., et al. 2010, *AJ*, **140**, 1830
- Gordon, Y. A., Boyce, M. M., O'Dea, C. P., et al. 2021, *ApJS*, **255**, 30
- Greene, J. E., Strader, J., & Ho, L. C. 2020, *ARA&A*, **58**, 257
- Grindlay, J. E., Heinke, C., Edmonds, P. D., & Murray, S. S. 2001, *Sci*, **292**, 2290
- Güdel, M. 2002, *ARA&A*, **40**, 217
- Guedel, M., & Benz, A. O. 1993, *ApJL*, **405**, L63
- Gültekin, K., King, A. L., Cackett, E. M., et al. 2019, *ApJ*, **871**, 80
- Hamilton, T. T., Helfand, D. J., & Becker, R. H. 1985, *AJ*, **90**, 606
- Harris, C. R., Jarrod Millman, K., van der Walt, S. J., et al. 2020, *Natur*, **585**, 357
- Harris, W. E. 1996, *AJ*, **112**, 1487
- Heinke, C. O., Grindlay, J. E., Edmonds, P. D., et al. 2005, *ApJ*, **625**, 796
- Hénault-Brunet, V., Gieles, M., Strader, J., et al. 2020, *MNRAS*, **491**, 113
- Hills, J. G. 1976, *MNRAS*, **175**, 1P
- Hunter, J. D. 2007, *CSE*, **9**, 90
- Husser, T.-O., Kamann, S., Dreizler, S., et al. 2016, *A&A*, **588**, A148
- Husser, T.-O., Wende-von Berg, S., Dreizler, S., et al. 2013, *A&A*, **553**, A6
- Johnson, H. M. 1976, *ApJ*, **208**, 706
- Johnson, H. M., Catura, R. C., Charles, P. A., & Sanford, P. W. 1977, *ApJ*, **212**, 112
- Kamann, S., Husser, T. O., Dreizler, S., et al. 2018, *MNRAS*, **473**, 5591
- Kamann, S., Wisotzki, L., & Roth, M. M. 2013, *A&A*, **549**, A71
- Knigge, C., Zurek, D. R., Shara, M. M., & Long, K. S. 2002, *ApJ*, **579**, 752
- Lingam, M. 2018, *MNRAS*, **473**, 1719
- Lu, T.-N., & Kong, A. K. H. 2011, *ApJL*, **729**, L25
- Maccarone, T. J. 2003, *A&A*, **409**, 697
- Maccarone, T. J. 2004, *MNRAS*, **351**, 1049
- Maccarone, T. J. 2005, *MNRAS*, **360**, L68
- Maccarone, T. J., Kundu, A., Zepf, S. E., & Rhode, K. L. 2007, *Natur*, **445**, 183
- Maccarone, T. J., & Servillat, M. 2008, *MNRAS*, **389**, 379
- Mann, C. R., Richer, H., Heyl, J., et al. 2019, *ApJ*, **875**, 1
- Martsen, A. R., Ransom, S. M., DeCesar, M. E., et al. 2022, *ApJ*, **941**, 22
- Masci, F. J., Laher, R. R., Rusholme, B., et al. 2019, *PASP*, **131**, 018003
- McConnell, D., & Ables, J. G. 2000, *MNRAS*, **311**, 841
- McConnell, D., Deacon, R., & Ables, J. G. 2001, *PASA*, **18**, 136
- McMullin, J. P., Waters, B., Schiebel, D., Young, W., & Golap, K. 2007, in ASP Conf. Ser. 376, *Astronomical Data Analysis Software and Systems XV*, ed. R. A., Shaw, F. Hill, & D. J. Bell, 127
- Merloni, A., Heinz, S., & di Matteo, T. 2003, *MNRAS*, **345**, 1057
- Miller, M. C., & Hamilton, D. P. 2002, *ApJ*, **576**, 894
- Miller-Jones, J. C. A., Strader, J., Heinke, C. O., et al. 2015, *MNRAS*, **453**, 3918
- Miller-Jones, J. C. A., Wrobel, J. M., Sivakoff, G. R., et al. 2012, *ApJL*, **755**, L1
- Nardiello, D., Libralato, M., Piotto, G., et al. 2018, *MNRAS*, **481**, 3382
- Paduano, A., Bahramian, A., Miller-Jones, J. C. A., et al. 2021, *MNRAS*, **506**, 4107
- Pellegrini, S. 2005, *ApJ*, **624**, 155
- Piotto, G., Milone, A. P., Bedin, L. R., et al. 2015, *AJ*, **149**, 91
- Plotkin, R. M., Markoff, S., Kelly, B. C., Körding, E., & Anderson, S. F. 2012, *MNRAS*, **419**, 267
- Plotkin, R. M., Miller-Jones, J. C. A., Chomiuk, L., et al. 2019, *ApJ*, **874**, 13
- Plotkin, R. M., Miller-Jones, J. C. A., Gallo, E., et al. 2017, *ApJ*, **834**, 104
- Pooley, D., Lewin, W. H. G., Homer, L., et al. 2002, *ApJ*, **569**, 405
- Portegies Zwart, S. F., Baumgardt, H., Hut, P., Makino, J., & McMillan, S. L. W. 2004, *Natur*, **428**, 724
- Portegies Zwart, S. F., & McMillan, S. L. W. 2002, *ApJ*, **576**, 899
- Rivera Sandoval, L. E., van den Berg, M., Heinke, C. O., et al. 2015, *MNRAS*, **453**, 2707
- Rivera Sandoval, L. E., van den Berg, M., Heinke, C. O., et al. 2018, *MNRAS*, **475**, 4841
- Roberts, M. S. E. 2013, in IAU Symp. 291, *Neutron Stars and Pulsars: Challenges and Opportunities after 80 Years*, ed. J. van Leeuwen (Cambridge: Cambridge Univ. Press), 127
- Rood, R. T., Turner, K. C., & Goldstein, S. J. 1978, *ApJ*, **225**, 804
- Salaris, M., Held, E. V., Ortolani, S., Gullieuszik, M., & Momany, Y. 2007, *A&A*, **476**, 243
- Sarajedini, A., Bedin, L. R., Chaboyer, B., et al. 2007, *AJ*, **133**, 1658
- Sault, R. J., Teuben, P. J., & Wright, M. C. H. 1995, in ASP Conf. Ser. 77, *Astronomical Data Analysis Software and Systems IV*, ed. R. A. Shaw, H. E. Payne, & J. J. E. Hayes (San Francisco, CA: ASP), 433
- Shishkovsky, L., Strader, J., Chomiuk, L., et al. 2018, *ApJ*, **855**, 55
- Shishkovsky, L., Strader, J., Chomiuk, L., et al. 2020, *ApJ*, **903**, 73
- Skrutskie, M. F., Cutri, R. M., Stiening, R., et al. 2006, *AJ*, **131**, 1163
- Strader, J., Chomiuk, L., Maccarone, T. J., Miller-Jones, J. C. A., & Seth, A. C. 2012a, *Natur*, **490**, 71
- Strader, J., Chomiuk, L., Maccarone, T. J., et al. 2012b, *ApJL*, **750**, L27
- Ströbele, S., La Penna, P., Arsenault, R., et al. 2012, *Proc. SPIE*, **8447**, 844737
- Sutanyo, W. 1975, *A&A*, **44**, 227
- Tasse, C., Hugo, B., Mirmont, M., et al. 2018, *A&A*, **611**, A87
- Terzian, Y., & Conklin, E. K. 1977, *AJ*, **82**, 468
- Tremou, E., Strader, J., Chomiuk, L., et al. 2018, *ApJ*, **862**, 16
- Tudor, V., Miller-Jones, J. C. A., Strader, J., et al. 2022, *MNRAS*, **513**, 3818
- Turk, P. J., & Lorimer, D. R. 2013, *MNRAS*, **436**, 3720
- Vahdat Motlagh, A., Kalemci, E., & Maccarone, T. J. 2019, *MNRAS*, **485**, 2744
- Weilbacher, P. M., Palsa, R., Streicher, O., et al. 2020, *A&A*, **641**, A28
- Wilman, R. J., Miller, L., Jarvis, M. J., et al. 2008, *MNRAS*, **388**, 1335
- Wilson, W. E., Ferris, R. H., Axtens, P., et al. 2011, *MNRAS*, **416**, 832
- Ye, C. S., Kremer, K., Rodriguez, C. L., et al. 2022, *ApJ*, **931**, 84
- Zhang, L., Ridolfi, A., Blumer, H., et al. 2022, *ApJL*, **934**, L21
- Zhao, Y., Heinke, C. O., Tudor, V., et al. 2020, *MNRAS*, **493**, 6033